J. Fluid Mech. (2014), *vol.* 742, *pp* 5–34. © Cambridge University Press 2014
doi:10.1017/jfm.2014.7

Adding in-line motion and model-based optimization offers exceptional force control authority in flapping foils

Jacob S. Izraelevitz† and Michael S. Triantafyllou

Department of Mechanical Engineering, Massachusetts Institute of Technology, Cambridge, MA 02139, USA

(Received 12 September 2013; revised 24 December 2013; accepted 25 December 2013; first published online 21 February 2014)

We study experimentally the effect of adding an in-line oscillatory motion to the oscillatory heaving and pitching motion of flapping foils that use a power downstroke. We show that far from being a limitation imposed by the muscular structure of certain animals, in-line motion can be a powerful means to either substantially augment the mean lift, or reduce oscillatory lift and increase thrust; propulsive efficiency can also be increased. We also show that a model-based optimization scheme that is used to drive an iterative sequence of experimental runs provides exceptional ability for flapping foils to tightly vector and keep the force in a desired direction, hence improving performance in locomotion and manoeuvring. Flow visualization results, using particle image velocimetry, establish the connection of distinct wake patterns with flapping modes associated with high lift forces, or modes of high thrust and low lift forces.

Key words: Biological fluid dynamics, swimming/flying, vortex shedding

1. Introduction

Most fast-swimming fish undulate their caudal fin in a symmetric fashion, with equal force generation from both the upstroke and downstroke of the fin. In contrast, other animals such as turtles and birds, flap their fins and wings in an asymmetrical fashion. This asymmetry typically involves a powerful downstroke generating large fluid forces and a 'feathering' upstroke with little force. Additionally, the flapping motion of the fin or wing is not purely transverse to the direction of motion of the animal, but also involves a strong oscillatory component parallel to its motion.

There are major differences on how the in-line component is employed in different animals: in turtle swimming, the flipper is moved both perpendicular to the flow, as in a traditional symmetric flap, but also with substantial motion parallel to the flow in the downstream direction (figure 1). This behaviour has been noted in unrestrained swimming turtles, such as *Chelonia mydas* (Davenport, Munks & Oxford 1984; Licht *et al.* 2010), and also in mollusk labriform swimmers such as *Clione limacina* (Szymik & Satterlie 2011). The significant motion parallel to the flow, or *in-line*

† Email address for correspondence: jsi@mit.edu

https://doi.org/10.1017/jfm.2014.7 Published online by Cambridge University Press

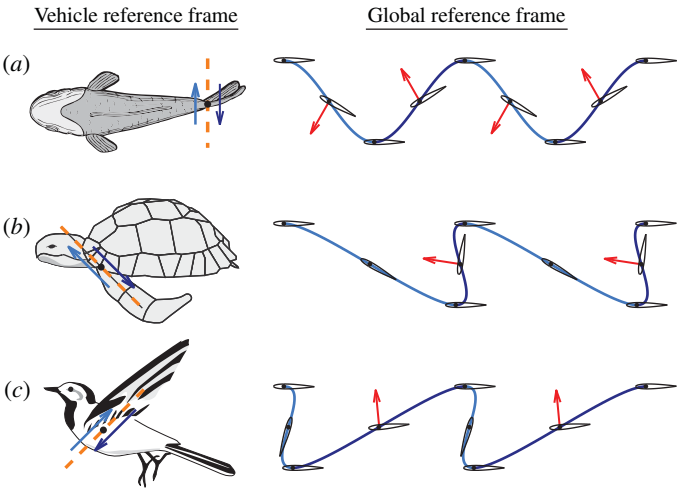


FIGURE 1. (Colour online) Comparison of (*a*) symmetric, (*b*) backwards in-line, and (*c*) forwards in-line motion. Various biological examples are able to change the direction of flapping foil force, simply by changing the orientation of flapping relative to oncoming flow. This degree of freedom, the stroke angle, is often ignored in experimental flapping foil studies, where the foil is constrained to flap only perpendicular to the flow. Animal art modified from public domain content at openclipart.org.

motion (Licht *et al.* 2010), rotates the instantaneous flow over the flipper, orienting the downstroke lift to produce large thrust and small transverse force. In addition, the angle of attack profile is changed to combine a powerful downstroke with a weak upstroke, creating a highly asymmetric flap that averages to a net thrust with little instantaneous transverse force. Previous experiments in Licht *et al.* (2010) have found that this mode of actuation generates less thrust than a symmetrically flapping foil, but it can actually improve efficiency while mitigating the undesirable transverse force effects.

Birds also exhibit significant in-line motion, but instead direct their flaps forward during the power downstroke, i.e. in the upstream direction (figure 1), thus augmenting the transverse force. Tobalske and Dial note that pigeons, magpies, and hummingbirds control their in-line motion as a function of airspeed, which they define using a stroke angle (Tobalske *et al.* 2007; Tobalske & Dial 1996). Substantial upstream in-line motion helps support the weight of the bird at low speed; however, at high speeds the in-line motion is reduced since weight is constant while lift scales with the square of velocity (Tobalske & Dial 1996; Berg & Biewener 2010). In-line motion also varies strongly with flight speed in bats (Lindhe Norberg & Winter 2006), a group with a very different evolutionary history than birds and subsequently different morphological constraints (Hedenström, Johansson & Spedding 2009). Robotic implementations of bat wings have demonstrated the effect of the stroke angle on leading-edge vortex structures (Koekkoek *et al.* 2012), adding further evidence to the importance of in-line motion to produce lift in flapping flight.

Among insects, the dragonflies, which have impressive manoeuvring abilities, exceeding those of other flying insects, also employ a variable, inclined stroke (Wakeling & Ellington 1997; DiLeo & Deng 2009).

https://doi.org/10.1017/jfm.2014.7 Published online by Cambridge University Press

Symmetrically flapping foil actuators, inspired by animal flight and swimming, can be used to generate both thrust and lift, and can be hydrodynamically efficient; experiments have reported thrust efficiencies up to 80% (Anderson *et al.* 1998; Prempraneerach, Hover & Triantafyllou 2003). Introducing a bias in the angular motion causes the development of steady lift, in addition to thrust, hence enabling manoeuvres (Read, Hover & Triantafyllou 2003; Schouveiler, Hover & Triantafyllou 2005). The oscillatory transverse forces that develop due to the unsteady flapping motion, however, constitute a disadvantage of such propulsors, in analogy to the rotating flow losses and breaking of symmetry introduced by rotary screw propellers.

Licht *et al.* (2010) showed that in the case of a turtle, the in-line oscillatory motion causes the fin force to have a large in-line component and a small transverse component, which is ideally suited to a neutrally buoyant animal in order to minimize transverse oscillations. Equally important, it was shown that its propulsive efficiency is equal to or better than that for a symmetrically flapping foil (without in-line oscillatory motion). Licht *et al.* (2010) showed further that in bird-like flapping, the in-line motion during the power stroke is in the opposite direction to that of the turtle, which results in substantially increased lift and serves to support the weight of the bird. As noted already, as the forward speed increases, a bird reduces the amplitude of its in-line motion, because the lift force scales with the square of the speed while its weight remains constant.

Hence, the added complexity of superposing an in-line oscillatory motion to a flapping foil is compensated by the ability to better control the direction of the produced forces to suit the function of the particular animal, without sacrificing propulsive efficiency. Such directional control ability is also very important for manoeuvring, especially when the animal must execute a sharp change of direction. In contrast, a symmetrically flapping foil always produces large transverse oscillatory forces, whose effect may be reduced by averaging out when in steady translation, but not when in transient motion, thus posing serious limitations in force direction control.

Figure 2 illustrates an example of a changing stroke angle to improve the force performance of a flapping foil. In this experiment, the foil is oscillated upstream during the first downstroke, and downstream during the third and fourth downstrokes. Data are taken from a smooth transition between optimized trajectories V and IV (see table 1 below), averaged over eight trials, experiment as described in § 2. The mean force coefficients change from a large, mainly transverse force, to a mostly in-line force, using a single transition cycle to smooth the different patterns in motion trajectories. Such a control scheme can be used on a flapping foil vehicle to provide augmented manoeuvrability on the timescale of individual flapping cycles.

In this paper we explore the possibility of enabling tight force control through optimization of the in-line motion of asymmetrically flapping foils. We show through a series of experiments on a high-aspect-ratio foil that both thrust and lift force can be controlled through in-line motion optimization. The use of active motion control can further enhance the performance of asymmetrically flapping foils, hence providing a prime means for tight force control, that can be used to significantly improve manoeuvrability.

2. Materials and methods

We conducted a series of tests on a high-aspect-ratio foil in order to explore the parametric range of an additional, in-line motion, combined with a power downstroke and feathering upstroke.

https://doi.org/10.1017/jfm.2014.7 Published online by Cambridge University Press

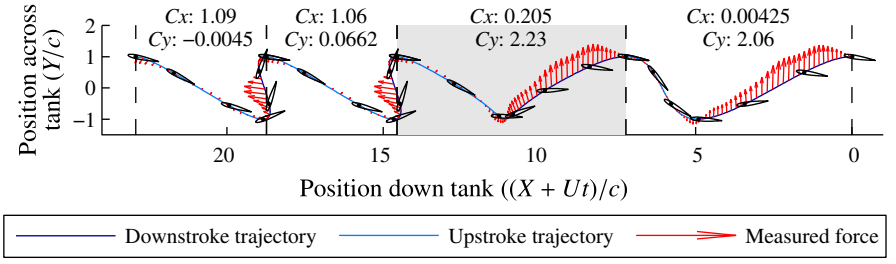


FIGURE 2. (Colour online) Using the stroke angle for force control. Experimentally measured force time trace during a manoeuvre where the stroke angle is changed from a bird-like trajectory, resulting in a large transverse force coefficient C_y, to a turtle-like trajectory providing only in-line force C_x. The instantaneous fluid force on the foil is indicated by the arrows, while the transition cycle is indicated by the grey region.

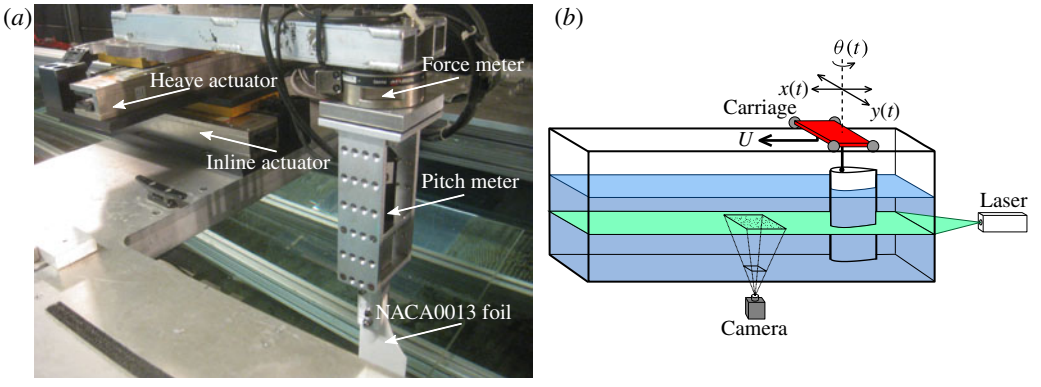


FIGURE 3. (Colour online) Towing tank schematic. (*a*) Photograph of the towing tank apparatus. The foil is attached to a pitch motor, which is mounted on the force meter. The entire assembly is then mounted on an two-axis linear stage. (*b*) The motion system rests on a carriage that moves down the tank at constant velocity U. A plane of particles in the flow is imaged from below the tank with a high-speed camera.

2.1. *Experimental apparatus*

We test a series of flapping trajectories on foils in a rectangular glass tank, 2.4 m long by 0.75 m width by 0.75 m depth, located in the MIT Towing Tank Facility. The towing apparatus is equipped with four actuators for controlling the motion of the foil (figure 3):

(*a*) a main carriage motor that tows the entire assembly at a constant speed U, through a chain drive mechanism that is tensioned by a pull-cord linear velocity transducer;
(*b*) a Parker Trilogy linear servomotor capable of moving the foil transverse to the flow, $y(t)$;
(*c*) a second Parker Trilogy linear servomotor that moves the foil in-line with the flow, $x(t)$, adding a time-varying velocity to the constant speed U;
(*d*) a rotary Yaskawa Sigma Mini Servomotor that actuates the foil pitch motion $\theta(t)$.

https://doi.org/10.1017/jfm.2014.7 Published online by Cambridge University Press

The x, y, and θ motors are controlled through a Delta Tau PMAC2A-PC motion controller, amplified by two Copley Controls XENUS Digital Drives and a Yaskawa Sigma Mini motor controllers respectively. The forces are measured with an ATI Gamma force transducer, logged through a LabVIEW interface. All data processing is performed in MATLAB. The foil is a lightweight NACA0013 carbon fibre blade, with a true chord length of 55 mm and aspect ratio of 6.5. The trailing edge of this foil is not perfectly sharp (0.6 mm width) due to manufacturing limitations, cutting approximately 3% off the ideal chord length. All data are filtered with a fifth-order low-pass Butterworth filter at 10 Hz to remove electrical and vibration effects without affecting the highest frequency fluid forces, usually the 6 Hz Strouhal shedding caused by the foil thickness.

The tank includes a movable false bottom, which was raised to within 8 mm of the foil tip, or 15% of the chord. The false bottom reduces the effect of the tip vortex (Slaouti & Gerrard 1981), which in addition to the presence of the free surface, allows us to approximate the fluid dynamics by two-dimensional unsteady foil theory. Therefore, while the nominal foil aspect ratio is 6.5, the effective aspect ratio is larger. Wave-making effects in previous experiments were found to be negligible at the carriage speed used, 0.2 m s^{-1}.

We visualize the foil wake using planar particle image velocimetry (PIV), illuminated by a Quantronix Darwin Nd:YLF laser (527 nm wavelength) located behind the foil. The laser is collimated and then expanded into a 4 mm thick plane, while the tank is seeded with 50 μm polyamid particles. A 10 bit Imager Pro HS CMOS high-speed camera, located below the tank facing upwards, records the flow at 600 Hz with 949 × 749 pixels. All PIV time-series processing is performed in LaVision DaVis 7.2 using the following parameters:

(*a*) three-frame gap to allow adequate seed motion;
(*b*) A 5 pixel sliding background pre-processing to remove unwanted reflections;
(*c*) three interrogation window passes, the first at 64 pixel and two at 32 pixels with 50% overlap;
(*d*) a post-processing vector median filter and a 3×3 smoothing filter.

An optical limit switch is located about halfway down the tank, which both triggers the PIV system and indexes the PIV dataset to the LabVIEW data log. Final data processing is performed in MATLAB, using the PIVMat toolbox to import the data.

2.2. *Parameterization of the flapping motion*

The foil is towed along the tank at constant speed U and is allowed to move in three degrees of freedom:

(*a*) motion transversely to the direction of towing, or heave $y(t)$;
(*b*) angular motion about a spanwise axis, or pitch $\theta(t)$;
(*c*) motion parallel to the direction of towing, or surge $x(t)$.

The surge and heave motions, $x(t)$ and $y(t)$, are set to be sinusoidal with the same frequency of oscillation. Their relative phase is set equal to zero, which is only an approximation of the observed animal motion, resulting in the foil translating back and forth along a straight line when viewed in the carriage's reference frame. We call this line the stroke line (figure 4), defined by an angle β with respect to the horizontal. The stroke line is the two-dimensional analogue of the stroke plane, a simplification used in several biological studies of flapping animals (Tobalske & Dial 1996; Lindhe Norberg & Winter 2006; Tobalske *et al.* 2007; Szymik & Satterlie 2011).

https://doi.org/10.1017/jfm.2014.7 Published online by Cambridge University Press

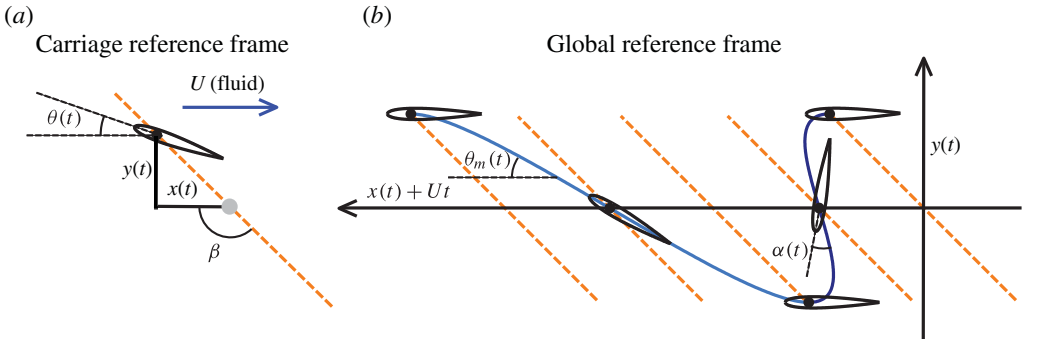


FIGURE 4. (Colour online) Definition of variables. (*a*) In the carriage reference frame, the foil travels along a single stroke line (illustrated by dashed line) with sinusoidal components as a function of time. This line is defined by the angle β with respect to the horizontal. (*b*) As the carriage moves at constant velocity U, the stroke line translates, resulting in a skewed-harmonic trajectory for the foil. Ignoring the induced velocities from the wake vortical patterns, the nominal angle of attack α is the angle between the foil pitch θ and the angle of foil motion θ_m.

The constant towing velocity U is analogous to the mean motion of the animal body, while $x(t)$ and $y(t)$ represent the foil motion relative to the body. This is of course an approximation: as the animal mass decreases relative to the foil force, the velocity U of a freely moving body will react appreciably to the instantaneous force on the foil rather than the mean force over several flapping cycles. However, this simplification limits the scope of the experimental parameter space, and correction factors can be applied for the unmodelled dynamics as discussed in § 4.

The motions in x and y are therefore given by the expressions:

$$y(t) = h\cos(2\pi f t), \tag{2.1}$$

$$x(t) = \frac{h}{\tan(\beta)}\cos(2\pi f t), \tag{2.2}$$

where h is the amplitude of the transverse motion, β is the stroke angle, and f is the flapping frequency (in Hz). Note that the above parameterization keeps the total transverse displacement at $2h$, independent of β. By assuming that the wake width is the same as the transverse displacement, we can thereby define a Strouhal number (Triantafyllou, Triantafyllou & Gopalkrishnan 1991):

$$St = \frac{2fh}{U}. \tag{2.3}$$

For symmetric flapping foil propulsion, high-efficiency thrust production occurs in wakes with a Strouhal number in the range of $0.2 < St < 0.4$, which also accurately predicts the flapping frequencies of various birds and swimming creatures (Triantafyllou, Triantafyllou & Grosenbaugh 1993; Taylor, Nudds & Thomas 2003; Nudds, Taylor & Thomas 2004). The Strouhal number is a wake parameter, based on the width of the wake, the frequency of oscillation and the speed of the forming jet. An analysis of the average velocity profile shows that the Strouhal number for optimal performance coincides with the frequency of maximum spatial amplification.

https://doi.org/10.1017/jfm.2014.7 Published online by Cambridge University Press

Moored *et al.* (2012) extended the principle of optimality for propulsion through the Strouhal number, employing the concept of hydrodynamic resonance that can be applied to three-dimensional flapping foils as well.

The angle of foil motion θ_m is dependent on the velocity of the foil in the global reference frame:

$$\theta_m(t) = \arctan\left(\frac{\dot{y}(t)}{\dot{x}(t) + U}\right). \tag{2.4}$$

The angle of the incoming flow relative velocity, θ_f, is influenced by the kinematics of the foil as well as the induced velocities from the vortical structures in the wake. For simplicity, we approximate θ_f with θ_m. The approximate angle of attack is, therefore:

$$\alpha(t) = \theta(t) - \theta_m = \theta(t) - \arctan\left(\frac{\dot{y}(t)}{\dot{x}(t) + U}\right). \tag{2.5}$$

Following Hover, Haugsdal & Triantafyllou (2004), we impose the functional form of the angle of attack, rather than that for the pitching motion. This was found to be significant for symmetrically flapping foils at high Strouhal numbers, when a sinusoidal pitch motion causes multiple peaks in the angle of attack and degradation of performance (Hover *et al.* 2004). It should be noted that an asymmetric flapping profile, where $\beta \neq 90°$, will not create a symmetric wake. We therefore set the intended angle of attack $\alpha(t)$ directly, discussed in detail in § 3, then derive the required $\theta(t)$ from the known $\theta_m(t)$:

$$\theta(t) = \alpha(t) + \arctan\left(\frac{\dot{y}(t)}{\dot{x}(t) + U}\right). \tag{2.6}$$

Using (2.1), (2.2) and (2.6), we parameterize the flapping trajectory first by setting the shape of $\alpha(t)$, and employing four dimensionless parameters (Strouhal number St, stroke angle β, heave to chord ratio h/c, and chord Reynolds number $Re = Uc/\nu$). We further limit these parameters to the following ranges that fit our experimental apparatus:

$$\left.\begin{array}{l} 0.1 < St < 0.5, \\ 45° < \beta < 135°, \\ h/c = 1, \\ Re = 11\,000. \end{array}\right\} \tag{2.7}$$

The constant heave to chord ratio is in accordance with the values that have been used in high-efficiency foils (Anderson *et al.* 1998), but it is only representative of animal motion, especially for three-dimensional flapping birds; however, this assumption keeps the parameter set small enough to focus on the in-line motion effects. Our chosen experimental Strouhal range overlaps with the expected high-efficiency and high-thrust flaps investigated in Anderson *et al.* (1998), while the stroke angle β is limited by the travel of the X-motion actuator. The Reynolds number of 11 000 was chosen to both fit the intended regime for biological propulsion and integrate easily into our existing tank equipment.

2.3. *Performance metrics*

In the experiments we conduct, we record the forces and define metrics for force production which can serve for parametric optimization.

https://doi.org/10.1017/jfm.2014.7 Published online by Cambridge University Press

2.3.1. *Foil forcing*

In each experiment, we recorded the following forces and moments on the foil as function of time:

$$F(t) = \begin{bmatrix} F_x(t) \\ F_y(t) \\ M_\theta(t) \end{bmatrix}, \tag{2.8}$$

where F_y is the transverse force, F_x is the thrust force, and M_θ is the torque about the rotation axis, after correcting for the acceleration of the mass/inertia of the experimental apparatus. We non-dimensionalize these forces using the dynamic pressure and reference foil area to find the following transverse and thrust force coefficients:

$$C_x(t) = \frac{F_x(t)}{0.5\rho U^2 S}, \quad C_y(t) = \frac{F_y(t)}{0.5\rho U^2 S}, \tag{2.9}$$

$$C_m(t) = \frac{M_\theta(t)}{0.5\rho U^2 Sc}, \tag{2.10}$$

where S is the projected area of the foil (one-sided), i.e. the span b times the chord c.

2.3.2. *Propulsive efficiency*

We compute the propulsive efficiency as the ratio of output power P_o to input or expended power, P_e, i.e. the product of average thrust times forward speed, divided by the average expended power:

$$\left.\begin{aligned} P_o(t) &= \frac{1}{T}\int_0^T F_x(t) U \,\mathrm{d}t, \\ P_e(t) &= \frac{1}{T}\int_0^T [F_x(t)\dot{x}(t) + F_y(t)\dot{y}(t) + M_z(t)\dot{\theta}(t)]\,\mathrm{d}t, \end{aligned}\right\} \tag{2.11}$$

$$\eta = \frac{P_o}{P_e}. \tag{2.12}$$

Previous experiments in Licht *et al.* (2010) have shown that downstream in-line motion can increase the propulsive efficiency of the flapping foil in the range $0.2 < St < 0.4$, with minor reduction in thrust.

Note that the output power P_o is not dependent on the transverse force $F_y(t)$. While the transverse force can be used for weight support in the case of flying animals, it is perpendicular to the constant free steam U and does no work. We therefore expect motion profiles intended to create large transverse forces, such as bird-like in-line motion, to have low propulsive efficiency by this definition. Turtle-like in-line motion, however, is expected to have high propulsive efficiency, given that the intended force is parallel to the free stream.

2.3.3. *Force quality: effectiveness of controlling force direction*

A principal reason for using in-line motion is to achieve better force control, in the sense of directing the force as desired and minimizing any components in the perpendicular plane. This is in principle particularly difficult in a flapping foil which is subject to large oscillatory forces.

Hence we define a metric of force quality as the magnitude of the parasitic force, which is perpendicular to the desired direction, expressed as the root-mean-square of

https://doi.org/10.1017/jfm.2014.7 Published online by Cambridge University Press

the undesirable force over the mean value of the total force. For example, in the case of a symmetric thrust-producing flap, the desired force is in the $\hat{x}$ direction. Therefore, we want to minimize the oscillation in F_y.

The following definition covers a wider range of flapping profiles: restricting the derivation to two dimensions, we express the instantaneous force in a reference frame consisting of the direction of intended force, defined through the unit vector $\hat{n}_i$, and the perpendicular direction. Ideally the flapping actuator would produce a force only in the direction of $\hat{n}_i$, and hence no force in the perpendicular direction:

$$\hat{n}_i = \begin{bmatrix} \hat{a}_1 \\ \hat{a}_2 \end{bmatrix}, \tag{2.13}$$

$$\begin{bmatrix} F_{\parallel}(t) \\ F_{\perp}(t) \end{bmatrix} = \begin{bmatrix} \hat{a}_1 & \hat{a}_2 \\ -\hat{a}_2 & \hat{a}_1 \end{bmatrix} \begin{bmatrix} F_x(t) \\ F_y(t) \end{bmatrix}, \tag{2.14}$$

where $F_{\parallel}(t)$ is the instantaneous force parallel $\hat{n}_i$, and $F_{\perp}(t)$ is the instantaneous force perpendicular to $\hat{n}_i$. We quantitatively judge the 'fitness' of the flapping profile by the root-mean-square (RMS) of $F_{\perp}(t)$, which we then normalize by the magnitude of the mean force, F_m:

$$\mathrm{RMS}(F_{\perp}) = \sqrt{\frac{1}{T}\int_0^T F_{\perp}(t)^2 \,\mathrm{d}t}, \tag{2.15}$$

$$\sigma^* = \frac{\mathrm{RMS}(F_{\perp})}{\|F_m\|}. \tag{2.16}$$

The non-dimensional metric σ^*, therefore, measures the magnitude of the unintended oscillatory forces relative to the magnitude of the intended force.

The σ^* metric rests on the assumption that zero-mean forces during the flapping cycle are wasted effort that vibrate the body unnecessarily, compared to the total mean force which actually guides the overall animal motion. Not all organisms necessarily attempt to minimize σ^*; it represents a force performance metric to be balanced with propulsive efficiency, power density, manoeuvrability of the mean force, or other actuator metrics. However, we choose to focus this paper on how different motion profiles affect σ^*, as it represents an important aspect of flapping foil propulsion not typically considered in the literature. Unlike traditional actuators, flapping foils create large oscillatory zero-mean forces, and these forces affect the performance independent of traditional actuator metrics.

3. Results

In this section, we explore the effect of the in-line motion parameters, starting with a symmetrically flapping foil and then proceeding with various shapes of in-line forcing, emulating the flapping motions of birds and turtles. We present results in detail of the first three different motion trajectories, enumerated in table 1, with the remainder discussed in § 5.

3.1. *Trajectory I – symmetric flapping profile*

As a basis for comparison, setting the stroke angle at $\beta = 90^\circ$ and $St = 0.3$ results in a symmetric flap similar to those studied extensively theoretically and experimentally

https://doi.org/10.1017/jfm.2014.7 Published online by Cambridge University Press

Trajectory name	Stroke angle β (deg.)	Strouhal number St	AoA profile
Trajectory I: no in-line motion	90	0.3	Sine max 25°
Trajectory II: upstream in-line	45	0.3	Cosine max 25°
Trajectory III: downstream in-line	135	0.3	Cosine max 25°
Optimized IV: mean $C_x = 1$, $C_y = 0$	135	0.48	Optimized
Optimized V: mean $C_x = 0$, $C_y = 2$	57	0.28	Optimized
Optimized VI: mean $C_x = 1$, $C_y = 4$	59	0.5	Optimized

TABLE 1. Motion trajectories.

(Theodorsen 1935; Triantafyllou *et al.* 1991; Anderson *et al.* 1998; Schouveiler *et al.* 2005; Hover *et al.* 2004). We impose a sinusoidal variation in the angle of attack α rather than for the pitching angle θ:

$$\alpha(t) = \alpha_{max} \sin(2\pi ft), \tag{3.1}$$

$$\theta(t) = \alpha(t) + \arctan\left(\frac{\dot{y}(t)}{\dot{x}(t) + U}\right). \tag{3.2}$$

For this trajectory, we set the maximum angle of attack to be $\alpha_{max} = 25°$. It should be noted that while 25° is higher than the recorded stall angle for a NACA0013 under steady towing conditions at this Reynolds number, unsteady foils can maintain lift at high angles of attack because of delayed stall effects (Maresca, Favier & Rebont 1978; Anderson *et al.* 1998).

Results for this symmetric flap are given in figure 5, averaged over five trials of two cycles each. The $\eta = 49\%$ efficiency is well within the range typically reported for experiments on symmetric flapping foils at similar maximum angle of attack and Strouhal number (Anderson *et al.* 1998; Schouveiler *et al.* 2005). Note that the thrust coefficient C_x contains two peaks, caused by the positive and negative lift on the downstroke and upstroke. Also note that there is substantial force perpendicular to the mean force direction: the transverse force C_y integrates to zero over a cycle, but its large oscillatory part can cause a vehicle to oscillate in heave and pitch. In this example, the non-dimensional oscillation cost $\sigma^* = 3.1$, so C_y has an RMS of 3.1 times the mean of C_x. As we show below, flaps that use in-line motion can be designed to have far smaller oscillation costs.

3.2. *Trajectory II – forward moving downstroke to augment transverse force*

Setting the stroke angle $45° < \beta < 90°$ results in a dramatic increase in the transverse force C_y during the downstroke, largely free of unwanted force oscillation. Figure 6 illustrates an example profile at $St = 0.3$ and $\beta = 45°$. There are many ways to define the $\alpha(t)$ profile over the course of the flapping motion, which can have a strong effect on the resultant force (Hover *et al.* 2004). For this example, we chose a single peaking profile for the downstroke. To effect a smooth transition between downstroke and upstroke, we use an offset cosine wave that blends well at the boundaries, defined by a single additional parameter α_{max}, which can be seen graphically in figure 6:

$$\alpha(t) = \begin{cases} \alpha_{max}(0.5 - 0.5\cos(4\pi ft)), & t \mod T \leqq T/2, \\ 0, & t \mod T > T/2, \end{cases} \tag{3.3}$$

https://doi.org/10.1017/jfm.2014.7 Published online by Cambridge University Press

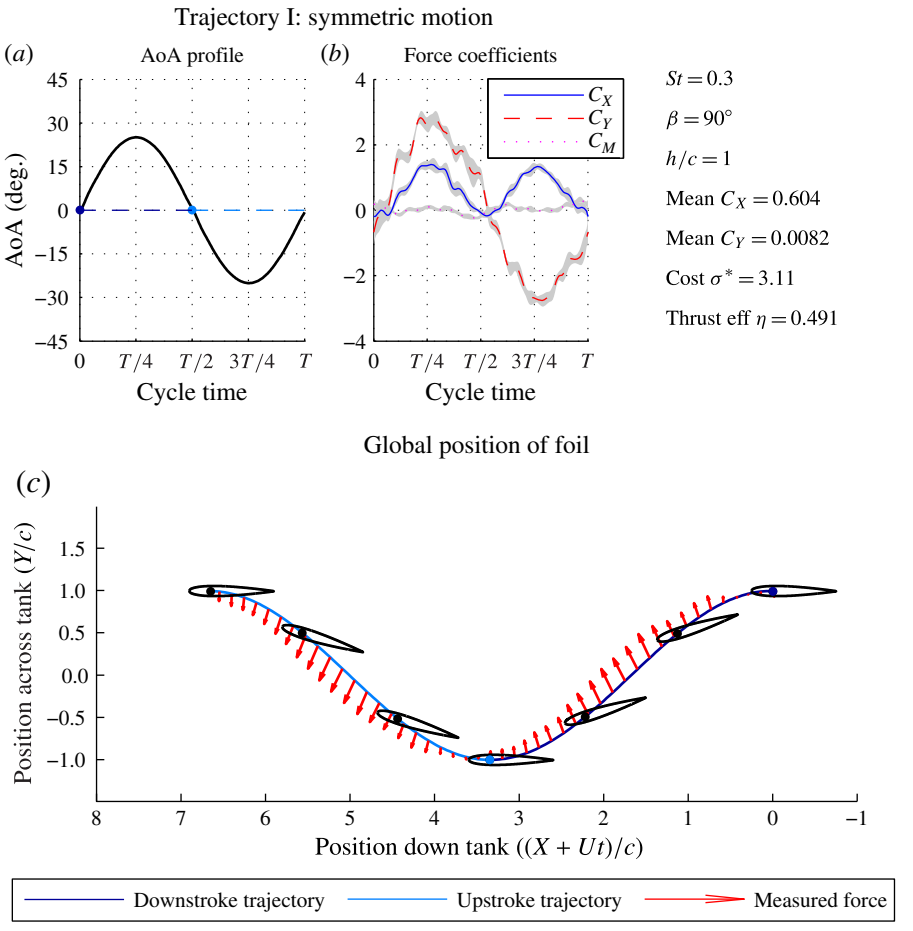


FIGURE 5. (Colour online) Trajectory I: symmetric flap. Experimental data for flapping perpendicular to the mean flow ($\beta = 90°$), at frequency given by $St = 0.3$. (*a*) The angle of attack, ignoring the wake-induced velocity, achieved by the θ motor. (*b*) The instantaneous force coefficients in the in-line and transverse directions (X and Y), normalized by $\rho SU^2/2$. All error bars (grey envelope) refer to one standard deviation over five runs of three flaps per run, while ignoring the first cycle in each run. The different parameters used to define the motion trajectory, along with the force performance of the flap, are shown on the right. (*c*) The force coefficient superimposed on the foil trajectory in the global frame, scaled to have a value of 10 for a vector length equal to the chord length. Foils are plotted every 1/6 of a flapping cycle.

where T is the flapping period, and $\alpha_{max} = 25°$ is the angle of attack at the middle of the downstroke.

As a general observation, flaps that involve forward in-line motion during the downstroke are easy to design and set up to exhibit good performance. The large lift, produced during the downstroke, is largely isolated in one direction in the global frame, hence removing the unwanted force oscillation present in a symmetric flap (in this example $\sigma^* = 0.28$). Note that there are small maxima and minima in the lift (figure 6) at the beginning and end of the upstroke when the foil rotates quickly; however, these are far smaller than the large values of the downstroke lift.

https://doi.org/10.1017/jfm.2014.7 Published online by Cambridge University Press

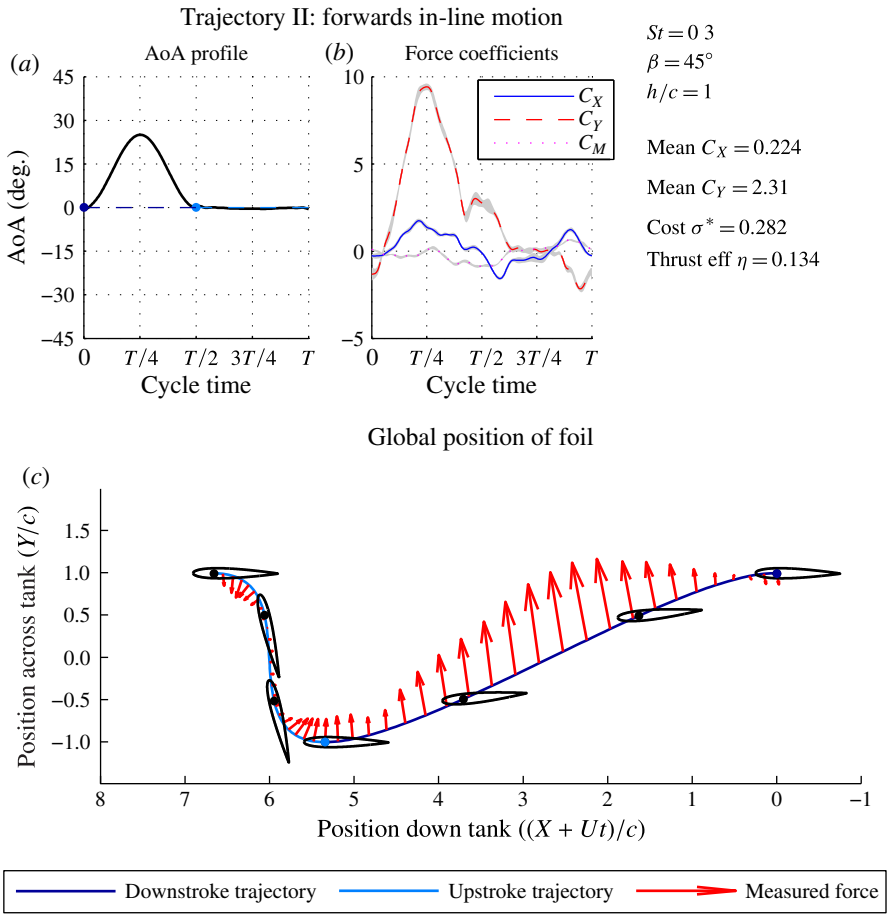


FIGURE 6. (Colour online) Trajectory II: bird-like forward biased downstroke. Experimental data for flapping forward during the downstroke, along an angle of $\beta = 45°$, with flapping frequency given by $St = 0.3$. Descriptions of the subplots are same as in figure 5. Note that lift production is almost entirely restricted to the downstroke; furthermore, the increased lift production boosts the transverse force C_y with little unwanted force oscillation in the thrust C_x.

The fact that lift is largely restricted to the downstroke for this specific motion trajectory is heavily supported by two-dimensional unsteady foil theory. According to this theory, the lift per unit span is dependent on three components: the quasi-steady lift, the added mass, and wake effects. If for the moment we focus only on the quasi-steady term, derived for a foil rotated at quarter-chord (Theodorsen 1935):

$$L_{qs}(t) = \frac{1}{2}\rho c v(t)\, 2\pi \left[v(t)\alpha(t) + \frac{c}{2}\dot{\theta}(t) \right], \tag{3.4}$$

where c is the chord, and $v(t)$ is absolute velocity in the global frame:

$$v(t) = \sqrt{\dot{y}(t)^2 + (U + \dot{x}(t))^2}; \tag{3.5}$$

https://doi.org/10.1017/jfm.2014.7 Published online by Cambridge University Press

$\dot{x}(t)$ and $\dot{y}(t)$ are given by the derivatives of (2.1) and (2.2):

$$\dot{x}(t) = -\frac{2\pi fh}{\tan\beta}\sin(2\pi ft), \quad \dot{y}(t) = -2\pi fh\,\sin(2\pi ft). \tag{3.6}$$

During the downstroke, $v(t)$ is larger than during the upstroke, since $\beta < 90°$ causes $\dot{x}(t)$ to be positive when $\sin(2\pi ft)$ is positive. In other words, in a bird-like flap, the foil is moving substantially upstream during the downstroke, meaning that the relative velocity of the foil is much higher. This can be verified visually in figure 6(*c*): the foils shown on top of the global motion trajectory are at constant time increments, illustrating the faster velocity during the downstroke.

Returning to (3.4), the quasi-steady lift is dominated by the angle of attack term $v(t)\alpha(t)$ during the downstroke, but $\alpha = 0$ during the upstroke, making the other term $(c/2)\dot{\theta}(t)$ dominant during the upstroke. However, since $\pi\rho Sv(t)$ is much smaller on the upstroke than on the downstroke, we have little quasi-steady lift on the upstroke compared to the downstroke. In effect, the foil is moving fastest when the largest forces are desired.

The unsteady lift due to wake effects and the added mass force additionally affects the total lift force. However, these effects are generally small compared to L_{qs} and also scale with the velocity of the foil $v(t)$, meaning they are dwarfed by the quasi-steady lift during the downstroke. As a result, the lift is largely isolated to the downstroke, as supported by the experiment.

The thrust efficiency is low, $\eta = 13\%$, as expected, as this motion has little mean thrust. The goal of this forwards-biased flap is to boost the transverse force by expending power, rather than boosting the thrust force.

3.3. *Trajectory III – backwards moving downstroke to augment thrust force*

Setting the stroke angle to the range $90° < \beta < 135°$, results in a thrust-producing flap, but the unsteady effects are far more pronounced. Figure 7 shows the analogous flap to the previous example, with $St = 0.3$, $\beta = 135°$, while $\alpha(t)$ is the same as in (3.3). Since the intended force direction for this flap is horizontal thrust, the transverse forcing at the beginning and end of the upstroke caused by the rapid foil rotation is undesirable, increasing σ^* and unnecessarily oscillating a hypothetical flapping foil vehicle. Additionally, the large negative thrust on the upstroke negates the effectiveness of the downstroke, caused by 'memory effects' in the wake, i.e. induced velocities from shed vorticity in the wake. Previous experiments in Licht *et al.* (2010) show similar peaks indicating strong wake memory effects during the upstroke.

The poor performance of this flapping mode can again be explained by analysing $v(t)$. Since $\beta > 90°$ instead, $v(t)$ is now smaller on the downstroke than on the upstroke, exactly opposite of what happens in the forward moving downstroke. Effectively, the foil is moving at its slowest when the intended force is highest, making this type of motion trajectory far more difficult to effectively design. The quasi-steady lift during the slow downstroke is now closer in magnitude to unsteady effects throughout the rest of the flap.

The propulsive efficiency of this motion profile is also low ($\eta = 27\%$) compared to the symmetric case (Trajectory I). Little thrust is developed as a result of the unwanted unsteady forces during the upstroke, and there is a large energy expenditure when the foil rapidly rotates.

Therefore, designing flaps that take advantage of backwards in-line motion is far more difficult, and significant correction is required to mitigate unsteady fluid

https://doi.org/10.1017/jfm.2014.7 Published online by Cambridge University Press

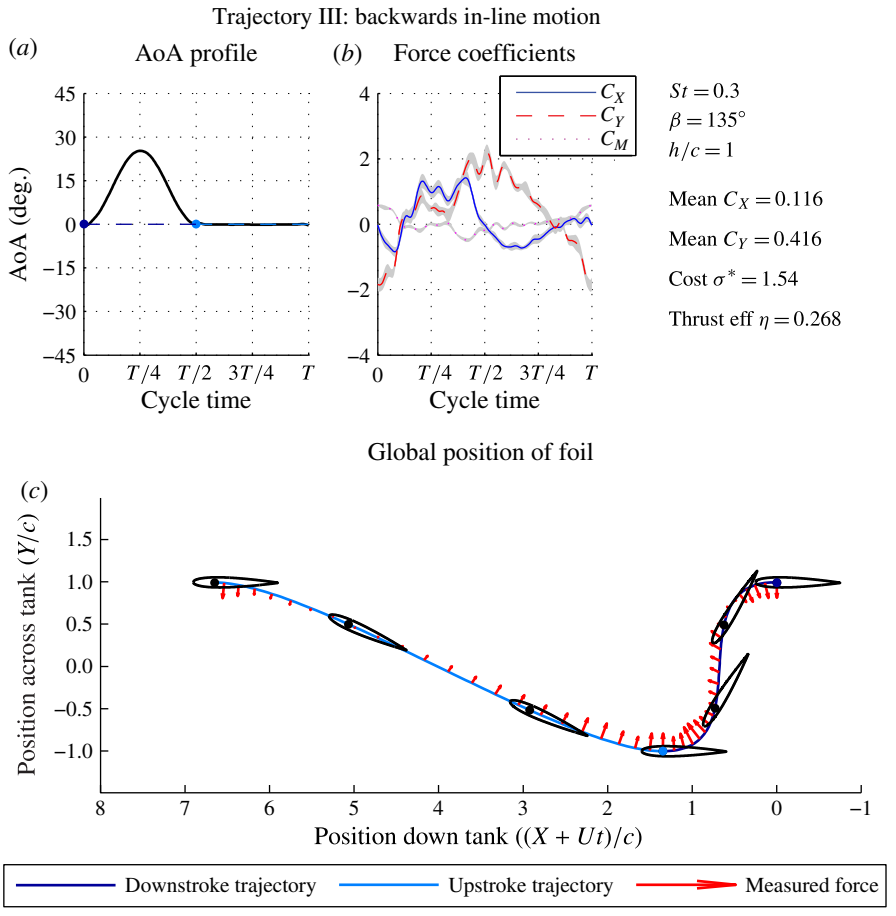


FIGURE 7. (Colour online) Trajectory III: turtle-like backwards moving downstroke. Experimental data for a backwards moving downstroke, along an angle of $\beta = 135°$, at frequency given by $St = 0.3$. Descriptions of the subplots are same as in figure 5. Note that unlike the bird-like flap, this flap is intended to create thrust C_x, not transverse force C_y. Accordingly, the large transverse forces at the beginning and end of the downstroke are unwanted, as is the negative thrust during the upstroke.

dynamics. As we show in the next section of this paper, the use of predictive control action alleviates all these problems.

4. Optimization and flapping parameter design

We show in this section that making relatively modest changes to the shape of the angle of attack curve as function of time over one period of oscillation, $\alpha(t)$, can effectively mitigate unwanted unsteady effects, so optimizing $\alpha(t)$ can lead to a clean force generation with minimized cost σ^*. Additionally, the stroke angle β and Strouhal number St have strong effect on the resultant mean flapping forces. We therefore set up an optimization routine that optimizes the shape of the angle of attack as well as the Strouhal number and stroke angle.

https://doi.org/10.1017/jfm.2014.7 Published online by Cambridge University Press

More specifically, we parameterize the problem in terms of the following $N + 2$ parameters to be optimized:

(*a*) stroke angle β;
(*b*) Strouhal number St;
(*c*) trajectory of the angle of attack $\alpha(t)$ as function of time, over N equidistant time instances, which is splined to create a continuous function.

4.1. *Optimization method*

Our intent is to demonstrate that optimization can yield far superior performance, hence we chose from simple methodologies that are adequate to obtain results with relatively few experiments. More specifically, we employ a model-based optimization driving iterative experimental runs. Another reason for choosing this methodology is that a large number of discretization points N are needed to properly parameterize a trajectory, hence the number of optimization parameters is too large to search the entire parametric space for a global optimum within a reasonable number of experimental trials. For example, even a coarse representation of $\alpha(t)$ into $N = 4$ parameters, and then discretizing each of the $N + 2$ parameters into 10 values, results in 10^6 experiments.

Several studies have been performed with optimization routines guiding systematic experiments or computational fluid dynamics (CFD) trials (Kern & Koumoutsakos 2006; Kaya & Tuncer 2007; Roberts *et al.* 2009), using algorithms such as weight perturbation (Jabri & Flower 1992) or CMA-ES (Hansen & Ostermeier 2001). However, these methods generally have far slower convergence when compared to model-based methods, where a theoretical model is used to guide the optimization between experimental trials. A disadvantage of model-based optimization is that the optimization engine can only make decisions informed by the model physics, which may not capture the full nature of the flow. The optimization may still reject disturbances from the unmodelled dynamics; however, it will only search in directions deemed favourable by the theoretical model.

Model-based optimization greatly improves the converge rate, since optimization gradients are calculated analytically instead of experimentally, but the optimality of the final result is dependent on the quality of the theoretical model. For the purposes of our design problem, however, the method is shown to design flaps that perform far better than the simple sinusoids described previously in § 2.2.

The optimization algorithm is therefore organized as follows:

(*a*) an initial flap is chosen based on the theoretical model, that meets a mean force vector constraint $F_{theoretical} = F_{desired}$, while minimizing the cost function $J = \sigma^*$;
(*b*) the initial flap is run through an experimental trial, recording the true forces $F_x(t)$ and $F_y(t)$;
(*c*) the initial flap shape is corrected using the theoretical model to predict how changes in the parameter space will change the measured $F_x(t)$ and $F_y(t)$ to the desired values, again minimizing the cost function $J = \sigma^*$;
(*d*) steps (*b*) and (*c*) are repeated until satisfactory convergence is obtained, defined in our case as when the measured force from the experiment is within 5% of the desired value $F_{desired}$.

The choice of model-based optimization algorithm is dependent on the nonlinearity and sparsity of the theoretical model dependences on the parameter space. For our optimization, we chose Sequential Quadratic Program for Nonlinear Constrained Optimization, or SNOPT, an algorithm described in Gill, Murray & Saunders (2005).

https://doi.org/10.1017/jfm.2014.7 Published online by Cambridge University Press

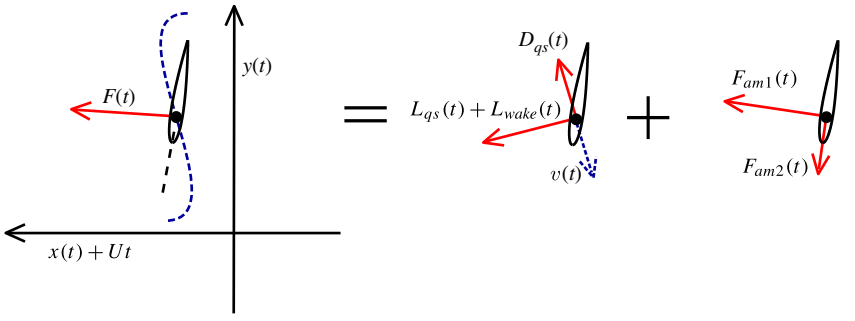


FIGURE 8. (Colour online) Force model. The four components of the force model are illustrated, along with their instantaneous directions. The lift and drag forces, $L_{qs} + L_{wake}$ and D_{qs}, are oriented with respect to the relative foil–fluid velocity, ignoring wake-induced velocities. The added mass forces, F_{am1} and F_{am2}, are represented in the foil-body frame.

The optimization code, along with its associated MATLAB wrapper, can be found at Philip Gill's website (Gill *et al.* 2005).

We choose to minimize the cost $J = \sigma^*$ rather than the expended power P_e or inverse efficiency $1/\eta$ to highlight the effect of in-line motion on providing exceptional force control, as previous studies have investigated the effect of in-line motion on efficient propulsion (Licht *et al.* 2010). Other cost functions are possible and fit within the framework of the optimization, depending on the performance goal of the flapping motion.

4.2. *Theoretical model used in the optimization*

We use a relatively simple theoretical model based on a blend of two-dimensional, linear, unsteady thin-airfoil theory, and a quasi-steady drag formulation:

$$F(t) = (L_{qs}(t) + L_{wake}(t))\hat{e}_L(t) + F_{am_1}(t)\hat{e}_1(t) + F_{am_2}(t)\hat{e}_2(t) + D_{qs}(t)\hat{e}_D(t). \tag{4.1}$$

These forces are illustrated in figure 8. The quasi-steady lift $L_{qs}(t)$ is given by (3.4), reprinted below, having direction $\hat{e}_L(t)$, which is perpendicular to the velocity $\boldsymbol{v}(t)$, and in the direction of the angle of attack:

$$\left.\begin{aligned} L_{qs}(t) &= \frac{1}{2}\rho c v(t)\, 2\pi \left(v(t)\alpha(t) + \frac{c}{2}\dot{\theta}(t)\right), \\ \hat{e}_L(t) &\times \boldsymbol{v}(t) = 0. \end{aligned}\right\} \tag{4.2}$$

The wake-induced lift $L_{wake}(t)$ of a small-amplitude flap is studied in the flutter theory literature, based on the classic results of Theodorsen (1935). The flapping motions considered in this paper exceed the linear range, since the amplitude of motion is comparable to the chord, $h/c = 1$, while there is also unsteady in-line velocity, i.e. $\dot{v}_x \neq 0$. A more detailed analysis of the effects of the vortical patterns, such as the model described in Pan *et al.* (2012), is therefore necessary to truly capture the wake effects. Minimizing a $J = P_e$ expended power cost, rather than a $J = \sigma^*$ oscillatory force cost, would probably require such an accurate wake model.

To mitigate the computational complexity of these wake models, we consider the wake-induced lift as a prime unmodelled dynamic quantity, and use a conservative simplification for the wake effects:

$$L_{wake}(t) \approx -\tfrac{1}{2}L_{qs}(t). \tag{4.3}$$

https://doi.org/10.1017/jfm.2014.7 Published online by Cambridge University Press

This simplification assumes that the Wagner effect (Wagner 1925) affects the lift magnitude for the entire flapping cycle, and ignores the phase information contained in the Theodorsen transfer function.

Hence, we proceed with this simplified model, because of its analytic tractability, and considered the omitted effects as unmodelled dynamics for the controller design. Using $J = \sigma^*$ force cost further supports this simplification, as modelled forces can be superimposed to mitigate unmodelled forces.

The added mass effects are given in the body frame, using the unit vectors $\hat{e}_1$ and $\hat{e}_2$, where $\hat{e}_1$ is parallel and $\hat{e}_2$ is perpendicular to the foil chord. The magnitudes of the added mass forces are:

$$\left.\begin{aligned} F_{am_1}(t) &= v_2(t)\dot{\theta}(t)m_{22} + \dot{\theta}(t)^2 m_{26}, \\ F_{am_2}(t) &= -a_2(t)m_{22} - a_\theta(t)m_{26}, \end{aligned}\right\} \tag{4.4}$$

where v_2, a_2, and a_θ denote the body-frame linear velocity, linear acceleration, and angular acceleration, respectively, expressed in the body-frame unit vectors $\hat{e}_1$ and $\hat{e}_2$. We neglect the nonlinear added mass term $\dot{\theta}(t)^2 m_{26}$ in this model to slightly simplify the computation, again withdrawing this term to the unmodelled dynamics. The added mass coefficients are approximated by a plate rotated at its quarter-chord, namely:

$$\left.\begin{aligned} m_{22} &= \tfrac{1}{4}\rho\pi c^2, \\ m_{26} &= -\tfrac{1}{16}\rho\pi c^3. \end{aligned}\right\} \tag{4.5}$$

The drag force is approximated by a quasi-steady drag equation, oriented in the direction $\hat{e}_D(t)$, opposing the instantaneous velocity, with magnitude:

$$D_{qs}(t) = \tfrac{1}{2}\rho c v(t)^2 C_D(\alpha), \tag{4.6}$$

where the coefficient of drag $C_D(\alpha)$ is approximated by a polynomial fit of experimentally measured steady drag force on the foil, illustrated in figure 9:

$$C_D(\alpha) = -3.70\alpha^6 + 2.08\alpha^4 + 2.52\alpha^2 + 0.0334. \tag{4.7}$$

We do not use a polynomial fit for the coefficient of lift C_L, since using the steady lift coefficient is a poor predictor of dynamic stall effects. Instead, as mentioned above in (4.3), we use an unsteady linear approximation for the lift coefficient and include a magnitude correction for wake effects. The theoretical lift coefficient is $C_L = 2\pi\alpha$, but we instead use $C_L = \pi\alpha$ to give a conservative approximation of wake effects, as predicted by Wagner's impulsive foil theory (Wagner 1925).

4.3. *Optimization constraints*

To automatically design flaps that meet all design criteria, we implement a number of constraints to guide the optimization routine.

(*a*) The mean of the predicted force component parallel to the direction of the desired force, $F_\parallel(t)$, is within 1% of the desired force magnitude.

(*b*) The mean of the predicted force component perpendicular to the direction of the desired force, $F_\perp(t)$, is less than 1% of the desired force magnitude.

(*c*) The jerk of $\theta(t)$ stays below a target value that scales appropriately with the flapping frequency and number of discretizations of t. This is easily implemented

https://doi.org/10.1017/jfm.2014.7 Published online by Cambridge University Press

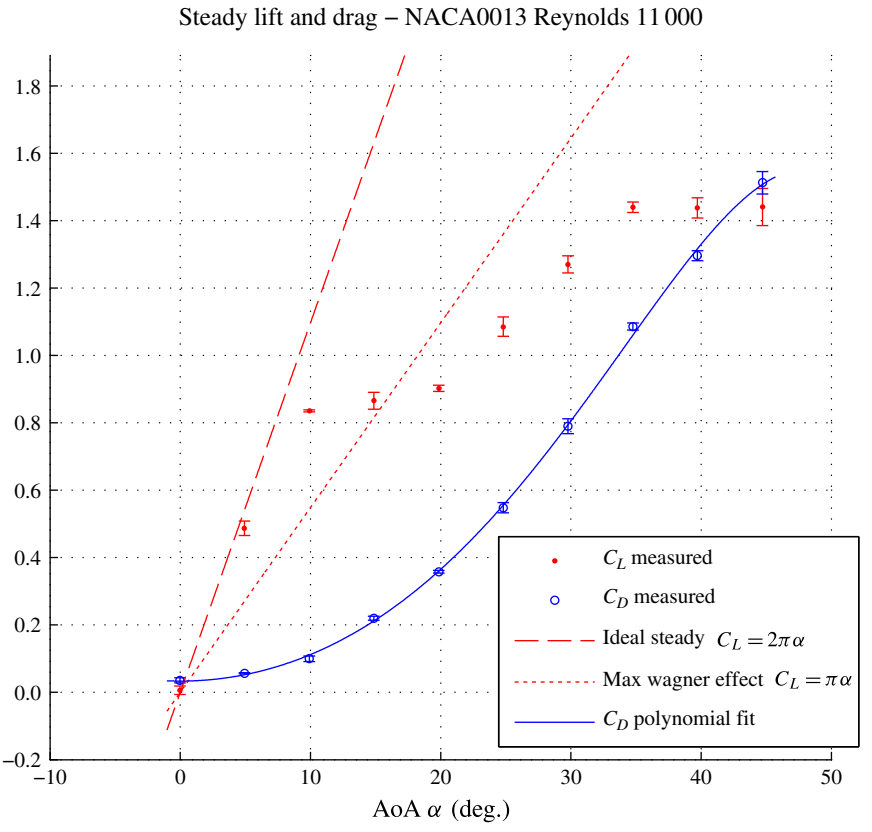


FIGURE 9. (Colour online) Steady force measurements on foil. Force data as the NACA0013 foil is towed at constant speed, averaged over three trials of 20 chord lengths of travel. Error bars refer to one standard deviation. The drag data are fitted to a polynomial for use in the theoretical drag model. The lift data are not fitted to a polynomial, as the steady lift coefficient is a poor predictor of unsteady lift at high angles of attack.

by keeping the triple difference $|\theta_k - 3\theta_{k+1} + 3\theta_{k+2} - \theta_{k+3}|$ below a given value. For our optimizations, we set this maximum value at $1/N$, in order to generate highly smooth motion trajectories.

(*d*) The angle of attack $\alpha(t)$ must stay below a maximum value to avoid full stall. In general, we found that a large α was necessary around $t = 0$ and $t = T/2$ to mitigate the additional lift caused by rotating the foil, while a smaller α was necessary during the rest of the trajectory. We therefore constrain the angle of attack between two offset cosine curves:

$$\left.\begin{aligned} &\alpha_{mid} = 25^\circ, \quad \alpha_{turn} = 45^\circ, \\ &\alpha_{max}(t) = (\alpha_{turn} - \alpha_{mid})\left[\tfrac{1}{2} + \tfrac{1}{2}\cos(2\pi ft)\right] + \alpha_{mid}, \\ &\alpha_{min}(t) = (\alpha_{turn} - \alpha_{mid})\left[-\tfrac{1}{2} + \tfrac{1}{2}\cos(2\pi ft)\right] - \alpha_{mid}, \end{aligned}\right\} \tag{4.8}$$

$$\alpha_{min}(t) < \alpha(t) < \alpha_{max}(t). \tag{4.9}$$

https://doi.org/10.1017/jfm.2014.7 Published online by Cambridge University Press

In addition, we filter the force data at a lower frequency for the optimization routine, using a fifth-order low-pass Butterworth filter at 5 Hz. This filter removes the force signature of the Strouhal shedding frequency caused by the boundary layer separation at the trailing edge, which occurs around 6 Hz. While the other forces on the foil can be mitigated through appropriate changes in the angle of attack of the foil, the forces due to the Strouhal shedding phenomena are uncontrollable. The lower frequency filter therefore mitigates this issue and improves convergence of the model-based corrections.

4.4. *Optimization results based on the theoretical model*

We verify the model performance in two ways: by comparison of the model and experimental force measurements, and by noting the direction of the predicted gradients of the parameters with respect to the true optimum. The latter of these evaluations is more significant, because it is more important that the model predict the correct direction, i.e. toward the optimum value, than provide a precise estimate of that optimal value.

First, we obtain the optimum values using only the theoretical model outlined in § 4.2, i.e. without conducting an experiment. Results are illustrated in figure 10, where the contour plots provide the value of the stroke angle β and Strouhal number St as functions of the required thrust and transverse force coefficients, C_x and C_y, respectively. The flapping pattern is defined by the same parameters as given in (2.7), except that instead of prescribing the angle of attack, $\alpha(t)$, as a harmonic function of time, it is instead parameterized by $N = 50$ discrete values at 50 equidistant time instants over one period of the flapping motion.

We note that optimized flaps for zero transverse force, i.e. along the $C_y = 0$ axis, require substantial backwards in-line motion ($\beta > 90°$) when the thrust constraint is also low. As the thrust constraint increases, however, it becomes increasingly more difficult to use only a power downstroke, without violating the maximum angle of attack constraint. As a result, the optimization chooses increasingly more symmetric flapping profiles, which incur higher oscillation costs. This result is in agreement with Licht *et al.* (2010), where backwards in-line motion was also found to modestly decrease the mean thrust.

As the required transverse force coefficient, C_y, increases, the model predicts increasingly larger forward flaps ($\beta < 90°$), capturing the features of bird-like flapping noted by Tobalske & Dial (1996).

The model also predicts the gliding regime, indicated by the dashed polar, which shows the performance of a NACA0013 foil in steady flow. As the intended C_x and C_y approach this regime, the predicted ideal Strouhal number decreases dramatically, as indicated by the slow flaps in the lower left corner of figure 10. The parameterization, however, eventually breaks down at such low Strouhal numbers – as St approaches zero, β no longer affects the flap – so the predicted ideal stroke angle varies erratically.

5. Optimization results using experiments

We proceed to derive optimized flapping patterns as outlined in § 4.1, i.e. using first the results of the theoretical model from the previous section, and then testing the foil experimentally. Based on an assessment of the experimentally measured performance of the foil relative to the prediction, we use the model to provide a new estimate, and continue alternating between experiments and model-based corrections,

https://doi.org/10.1017/jfm.2014.7 Published online by Cambridge University Press

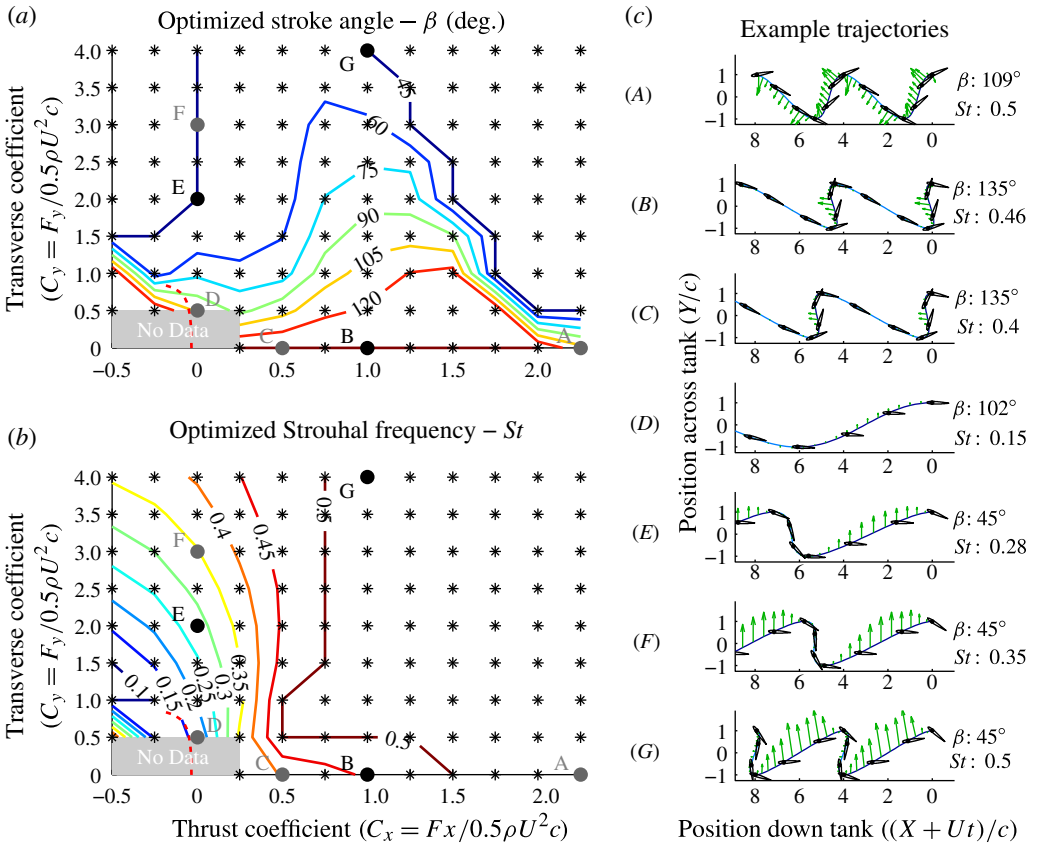


FIGURE 10. (Colour online) Parameter selection using only the theoretical model. Optimized flapping patterns using the theoretical model only. A flapping pattern was derived for every point marked with an asterisk (*), based on 52 parameters (stroke angle β, Strouhal number St, and 50 equidistant time intervals for the angle of attack over one period $\alpha(t)$). (*a*) Contour plot indicating the stroke angle β, with 45° implying forward, bird-like in-line motion, while 135° is for backwards, turtle-like in-line motion. (*b*) Contour plot indicating the designed flapping frequency. (*c*) Illustrations of a few of the designed trajectories, indicating their β, St, $\alpha(t)$, and predicted force performance. The polar for a NACA0013 in steady flow is given by the dashed curve in the lower left corners of (*a*) and (*b*) (taken from figure 9).

until convergence is obtained. We selected the results from optimizations B, E, and G in figure 10, and further optimize them using experiments to design optimized trajectories IV, V, and VI respectively.

5.1. *Optimized trajectory IV – intended* $C_x = 1$, $C_y = 0$

An example optimization progression for a thrust-producing flap is illustrated in figure 11, with required mean thrust coefficient $C_x = 1$ and transverse force coefficient $C_y = 0$.

The initial flapping pattern, taken from optimization B of figure 10, provides results not far from the desired values, but the unaccounted effects provide a relatively large mean unwanted force C_y. It should be noted that this initial flap performs far better

https://doi.org/10.1017/jfm.2014.7 Published online by Cambridge University Press

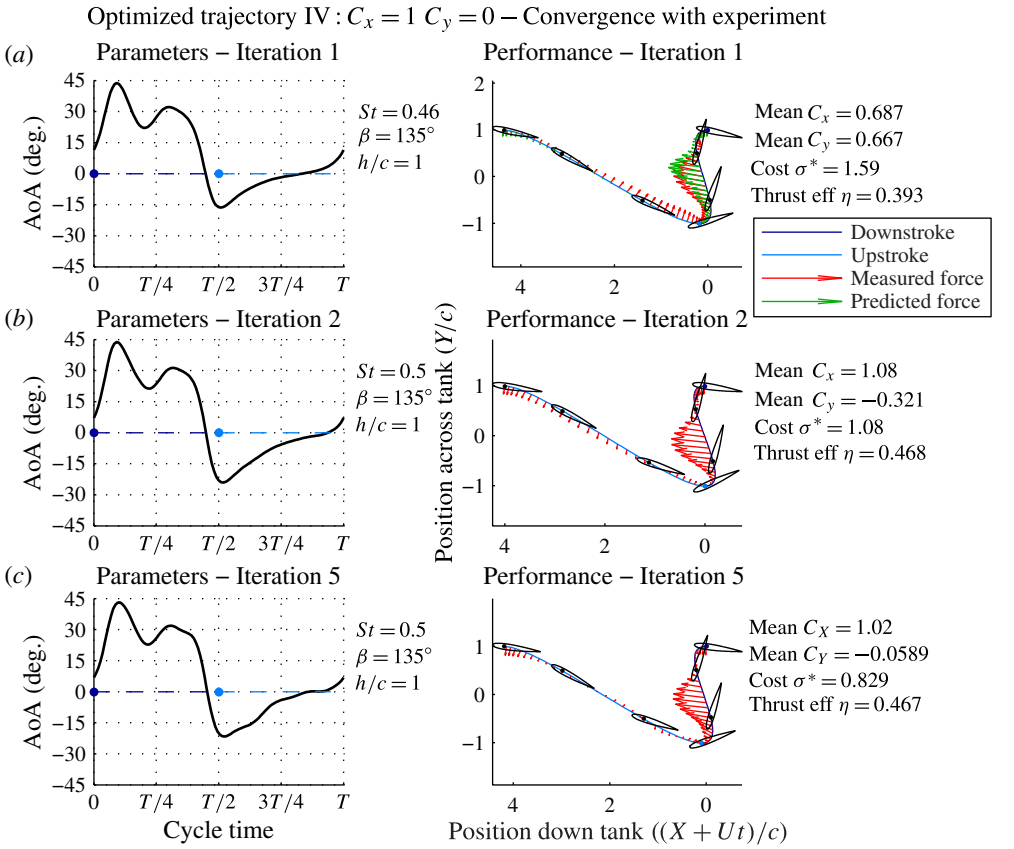


FIGURE 11. (Colour online) Optimization IV using experiments $C_x = 1$, $C_y = 0$. Each row of the figure refers to an iteration of the optimization process. The left plots illustrate the angle of attack and flapping parameters, while the right plots depict the motion and force performance. (*a*) The optimization begins with the results of figure 10, designed for the required $C_x = 1$ and $C_y = 0$. The top right plot depicts the expected force from the model and the force measured from the experiment. (*b*) On the basis of the difference between measured and predicted force, a new flap is designed, which is shown in the middle plots. (*c*) After five such iterations, the force performance has suitably converged.

than the simple flaps described in § 3.3. Compared to the flap in figure 7, the angle of attack has been altered to mitigate much of the unwanted lift at the beginning and end of the downstroke, indicated by the peaks and troughs in the angle of attack $\alpha(t)$, largely restricting the lift to the middle region of the downstroke. The overall mean force, however, has a large bias towards positive C_y since the model does not adequately predict the wake-induced lift.

By assessing the difference between the predicted and experimentally measured forces, the theoretical model is used to provide a correction to the original design; the new design is tested again and the prediction is assessed against the new experimental results; and hence a new correction is derived, until convergence is obtained. For example, the second designed flap mitigates most of the unwanted C_y (figure 11*b*). After five iterations of experimental runs and model-based corrections, the design converges to within 5% of the desired mean force.

https://doi.org/10.1017/jfm.2014.7 Published online by Cambridge University Press

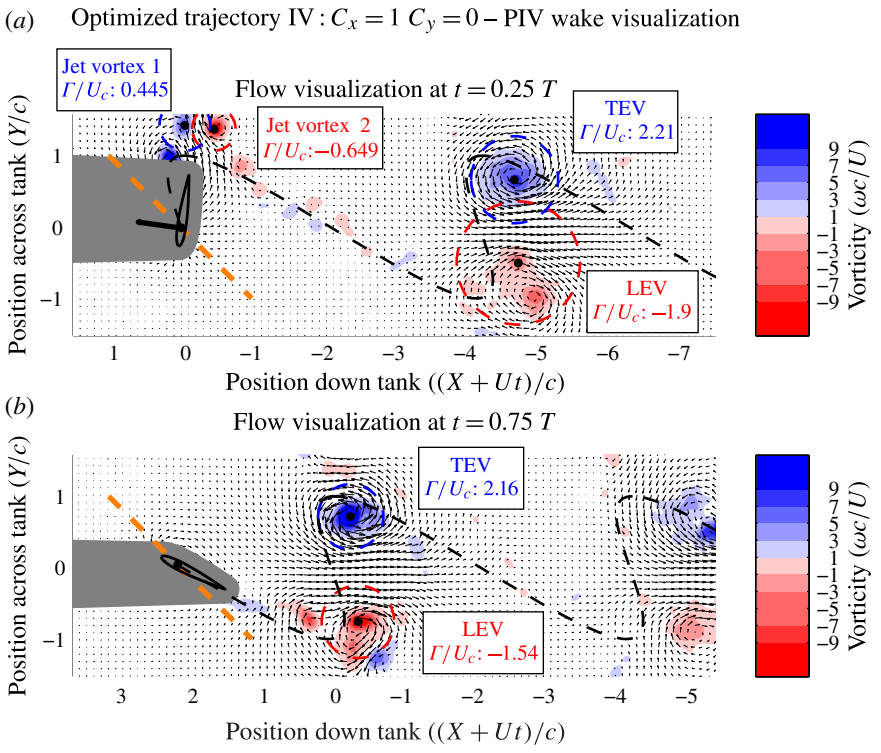


FIGURE 12. Flow visualization on optimized trajectory IV, $C_x = 1$, $C_y = 0$. The phase-averaged PIV data illustrate the wake structure at (*a*) $t = 0.25T$ (midway through the downstroke) and (*b*) $t = 0.75T$ (midway through the upstroke). The shadow of the foil in the laser plane is coloured in grey, in addition to a two interrogation-window-thick region around the foil. The stroke plane, which moves to the left at velocity U, is highlighted by an orange dashed line, while the black dashed line indicates the trajectory of the foil. The black arrow coming out of the foil quarter-chord point denotes the instantaneous fluid force coefficient, scaled to have a value of 10 for a length equal to the chord length. Velocity vectors normalized by U, scaled by 1/5, and spatially under-sampled by 1/2 for image clarity.

Remarkably in this optimization, minimizing the cost σ^* also unintentionally increases the efficiency η from 39% to 47%. The intuitive explanation for this is that mitigating the zero-mean forces can decrease the expended power; however, power must also be expended to rotate the foil to change the angle of attack and instantaneous lift. Regardless, the efficiency of this in-line-motion flapping trajectory now far exceeds the naive sinusoidal trajectory III and competes with the symmetric case trajectory I while effectively mitigating the unwanted oscillating forces.

Figure 12 gives a detailed view of the wake of this final optimized trajectory, obtained from phase-averaged PIV data. The number of averaged datasets ranges from four on the far-left and -right edges of the PIV image, to eight datasets in the centre.

A trailing-edge vortex (TEV) is shed as the foil accelerates into the downstroke, and indicates that the foil has developed 'bound' vorticity that provides the downstroke lift. The leading-edge vortex (LEV) grows and is shed at the end of the downstroke. The leading- and trailing-edge vortices lie along the same transverse line, at a transverse

https://doi.org/10.1017/jfm.2014.7 Published online by Cambridge University Press

distance from each other to form a rearward facing pulsed jet (figure 12*b*), hence providing a large thrust force with very little transverse force.

Additionally, two smaller vortices are shed as the foil rotates quickly during the upstroke/downstroke transition (figure 12*a*), creating a small secondary jet. The transverse force from the secondary jet is also experimentally recorded (figure 11*c*) at the end of the upstroke. This transverse force is considered high σ^* cost, but its mean force contribution is offset by the slight upwards angle of the downstroke lift.

Vortex circulation values, shown in figure 12, are calculated by summing all the vorticity of the same sign contained within a circular region, effectively allowing for overlapping regions of opposite-signed vorticity. These circular regions are centred on a local maximum or minimum in the vorticity field, and are radially dilated until the mean vorticity on the perimeter is 5% of the vorticity in the centre (Epps & Techet 2007).

5.2. *Optimized trajectory V – intended* $C_x = 0,\ C_y = 2$

Using a similar process as employed in the previous section, the theoretical model is first used to design an initial trajectory, then used again to provide incremental corrections to experimental results, eventually converging to a motion trajectory with the intended mean force of $C_x = 0$ and $C_y = 2$.

As illustrated in figure 13, the theoretical model in optimization E initially underestimates the downstroke lift, but otherwise accurately predicts the force performance. In this case, we needed a longer iterative process to achieve convergence, requiring eleven trials, to get as close as possible to a zero-mean thrust. The propulsive efficiency η is essentially zero, given there is no mean thrust from the motion trajectory.

The PIV wake visualization of this optimized trajectory is provided in figure 14. Similar to the trajectory optimized in the previous case, trailing-edge vorticity is shed as the foil accelerates into the downstroke, indicating bound vorticity on the foil that provides the downstroke lift. However, the trailing-edge vorticity is distributed throughout the downstroke (figure 14*a*), unlike in an impulsively started foil where a lump vortex is formed; this means that the wake-induced velocity is smaller and the lifting force builds more quickly than would be expected from the Wagner effect (Wagner 1925).

A large foil-bound leading-edge vortex provides additional lift force. The LEV is shed in the wake at the end of the downstroke (figure 14*b*) and interacts destructively with new trailing-edge vorticity also shed at the end of the downstroke. In the far wake, this destructive interaction and vortex wrap-up leaves only a single large TEV, resembling the wake of a foil started impulsively from rest (Wagner 1925).

5.3. *Optimized trajectory VI – intended* $C_x = 1,\ C_y = 4$

Figure 15 demonstrates the final optimized trajectory with intended thrust coefficient of $C_x = 1$ and transverse coefficient of $C_y = 4$. This experiment uses optimization G of figure 10 as a first estimate.

This trajectory, in particular, highlights the importance of in-line motion for augmenting the foil lift. For example, a lift coefficient of $C_L = 4$ is not possible on a typical steady foil: assuming the theoretical $C_L = 2\pi\alpha$, a steady foil would require an angle of attack of $\alpha = 36°$, which is well-beyond the stalling angle of a NACA0013 (figure 9). Lift augmentation in this case is possible because of the

https://doi.org/10.1017/jfm.2014.7 Published online by Cambridge University Press

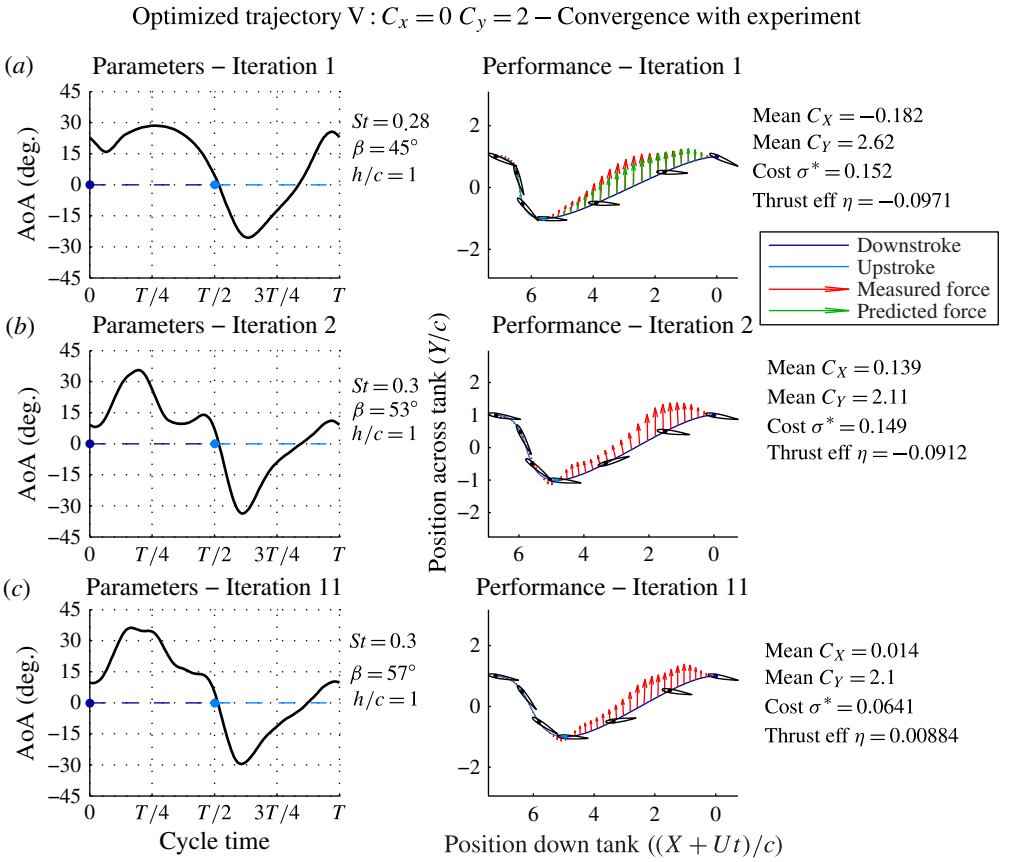


FIGURE 13. (Colour online) Optimization V using experiments, $C_x = 0$, $C_y = 2$. Similar to figure 11, each row refers to an iteration of the optimization process. (*a*) The top row indicates the flap designed through the model-only optimization described in figure 10. (*b*) On the basis of the difference between measured and predicted force, a new flap is designed, using the model described in § 4.2. (*c*) After a number of such iterations, the force performance has suitably converged.

in-line motion, which allows the foil to move faster than the mean flow, in addition to delayed stall effects from the pulsed angle of attack (Dickinson & Gotz 1993).

If in-line motion were employed without any motion transverse to the flow, then this large lift coefficient would come at the cost of increased drag. However, the transverse motion of the foil expends energy to generate the thrust necessary to offset that drag. In this optimization, the net thrust is actually positive ($C_x = 1$). This manoeuvre would be especially important for the quick launch of an autonomous aerial vehicle, where maintaining a large lift coefficient and adequate thrust coefficient is necessary given the slow speed of the aircraft.

As indicated in figure 15, the optimization routine again underestimates the downstroke lift, but converges suitably after a number of corrections to provide the desired force value. Similar to optimized trajectory IV, the thrust efficiency η again increases unintentionally over the course of the optimization as σ^* is minimized. The final trajectory achieves a low oscillatory cost $\sigma^* = 0.135$ and a propulsive efficiency of $\eta = 19\%$, while boosting the transverse force to $C_y = 4$.

https://doi.org/10.1017/jfm.2014.7 Published online by Cambridge University Press

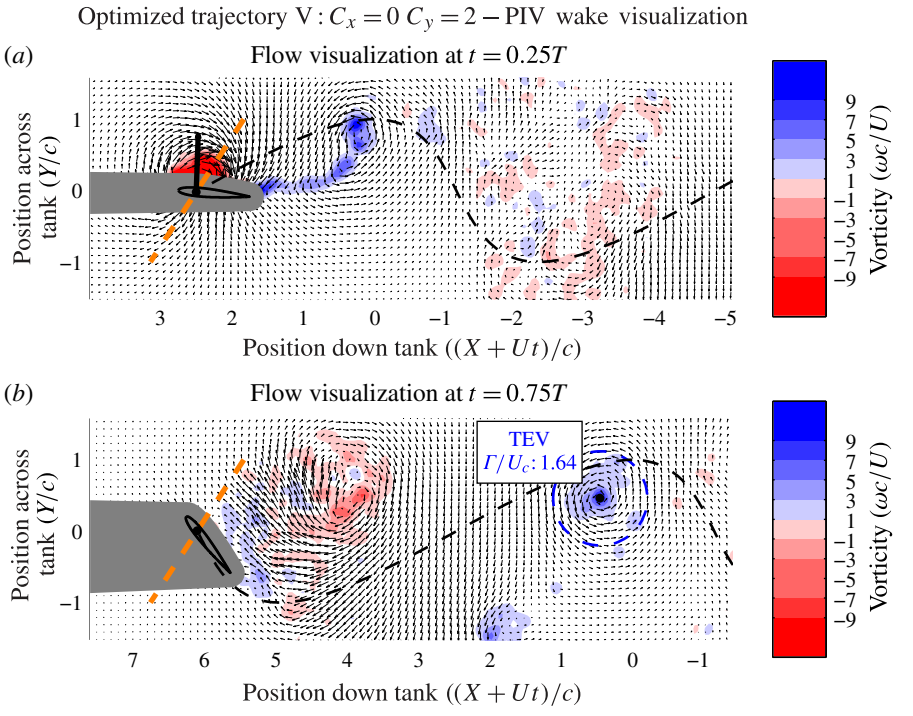


FIGURE 14. Flow visualization on optimized trajectory V, $C_x = 0$, $C_y = 2$. Similar to figure 12, the PIV data illustrate the wake at (*a*) $t = 0.25T$ and (*b*) $t = 0.75T$. Scaling identical to figure 12.

The foil wake is demonstrated in figure 16. The wake initially consists of trailing-edge vorticity, shed gradually and hence distributed throughout the downstroke, similarly to optimized trajectory V. A bound LEV augments the lift during the downstroke (figure 16*a*). Unlike optimized trajectory V, this leading-edge vortex does not interact destructively with trailing-edge vorticity at the beginning of the upstroke. Instead, we can see a smaller vortex form from the trailing edge, lying above the shed LEV and forming with it a jet flow (figure 16*b*). This jet is associated with the thrust force that has been generated during the downstroke.

Optimized trajectory VI, therefore, has a wake that combines aspects of both previous optimizations: a jet flow to provide the thrust, similar to the only-thrust case (optimized trajectory IV), and a large TEV indicating a large lifting force during the downstroke, similar to the only-transverse-force case (optimized trajectory V).

6. Conclusions

We show experimentally that birds and certain marine animals that actuate their flapping foils with substantial in-line motion can enjoy a substantial benefit in terms of improved force vectoring and control, without necessarily sacrificing efficiency.

When animals employ in-line oscillation they also use a power downstroke and a feathering upstroke. Depending on the direction of the in-line motion during the downstroke, the resulting force can be made to consist of mainly a thrust force with small oscillatory lift, as in turtles and mollusks, or of a large lift component in

https://doi.org/10.1017/jfm.2014.7 Published online by Cambridge University Press

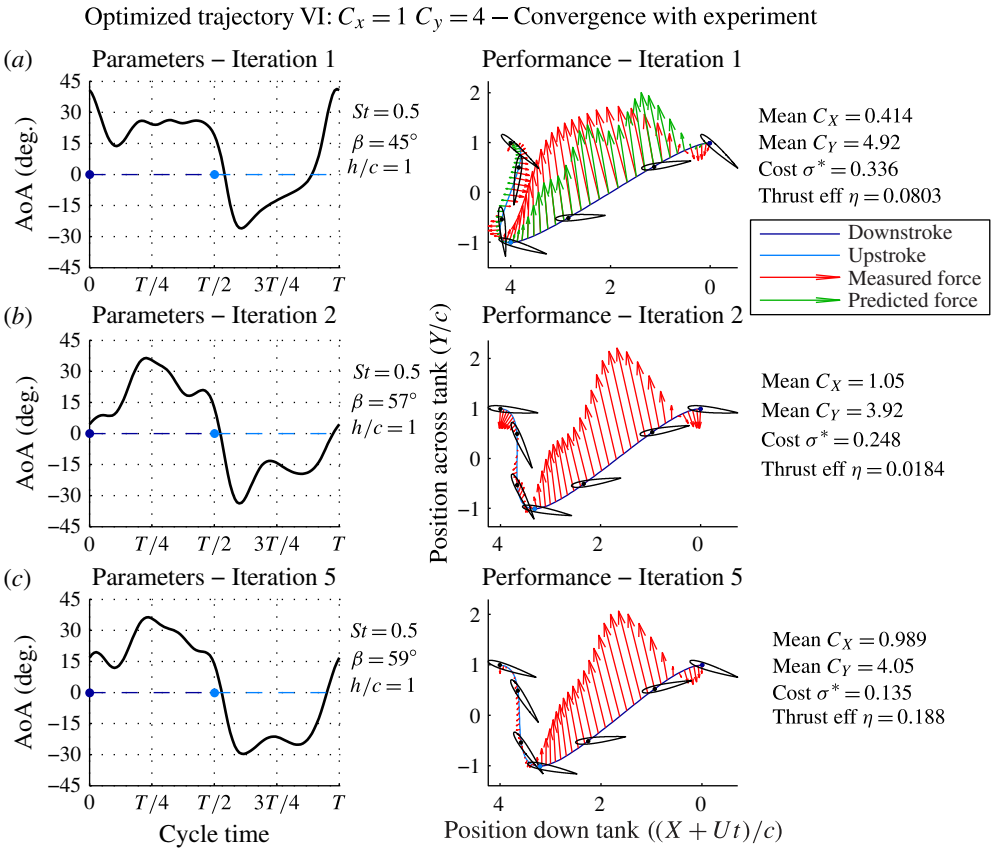


FIGURE 15. (Colour online) Optimization VI using experiments, $C_x = 1$, $C_y = 4$. Similar to figure 11, each row refers to an iteration of the optimization process. (*a*) The top row indicates the flap designed through the model-only optimization described in figure 10. (*b*) After five iterations of improving the experiment, based on the difference between the measured and predicted force, the mean force converges to the desired value (*c*).

addition to thrust, as in birds. The ratio of thrust to lift force can be chosen arbitrarily by adjusting the in-line-motion parameters.

In the case of large thrust generation, we show that the principal restriction is in the maximum angle of attack, to prevent excessive dynamic stall. Although the maximum angle of attack can be significantly higher than the stalling angle for a foil moving at constant angle of attack, a reasonable upper limit still exists around 25° for high-aspect-ratio foils. We find that as the specified thrust force is increased for a fixed maximum angle of attack, the optimization tends increasingly towards a symmetric flapping, i.e. involving little in-line motion and a power upstroke.

In the case of large lift generation, a forward in-line motion during the power stroke can be used to increase the mean lift far beyond the value obtained for a steadily moving foil. The high maximum angle of attack does not cause stall due to delayed stall effects, while the increased relative foil–fluid velocity further boosts the lift force. This extra lift could be especially useful for engineering applications of unsteady foils.

Added complexity is introduced when using in-line motion, both in terms of having an extra degree of freedom to actuate, and because several parameters must

https://doi.org/10.1017/jfm.2014.7 Published online by Cambridge University Press

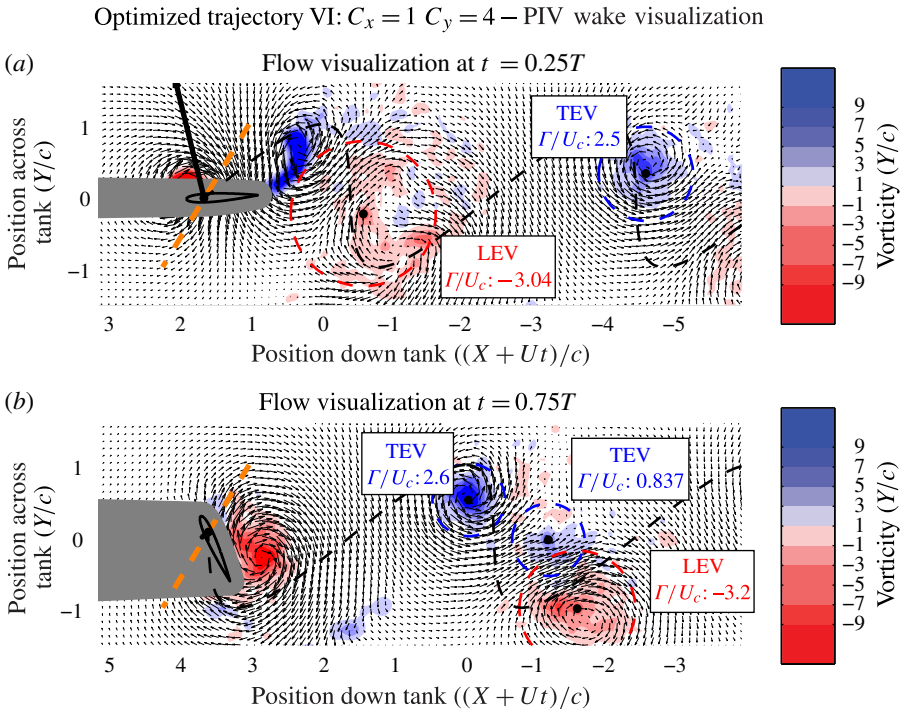


FIGURE 16. Flow visualization on optimized trajectory VI, $C_x = 1$, $C_y = 4$. The PIV data are phase averaged at (*a*) $t = 0.25T$ and (*b*) $t = 0.75T$, i.e. the middle of the downstroke and the middle of the upstroke, respectively. Scaling identical to figure 12.

be optimized: the unsteady motion, even under steady-state conditions, is not purely sinusoidal, while strong effects from the vortical patterns in the wake require special modification of the motion profile. Such optimization is especially needed when a low lift force is commanded, as the overall force is very sensitive to the functional shape of the angle of attack versus time: unsteady wake effects become significant, because of the large difference in the relative foil–fluid velocity in the downstroke versus the upstroke.

We show that such an optimization scheme is very effective when employing a model-based iterative optimization method. A simplified theoretical force model is used to drive an iterative process, altering the parameters of the flapping foil trajectory based on the difference between the theoretical predictions and experimental results. The process is shown to converge, leading to the generation of forces in the desired direction and with very small undesirable forces. The parameters of the trajectory consist of the Strouhal number, stroke angle, and the profile of the angle of attack as functions of time; the latter is specified at N points along one period of oscillation, where typically $N = 50$. Three examples of optimized flapping foils have been worked in detail:

(*a*) optimized trajectory IV, a turtle-like case, with specified thrust coefficient $C_x = 1$, and zero lift coefficient $C_y = 0$;

(*b*) optimized trajectory V, a purely lifting foil, with zero specified thrust coefficient $C_x = 0$, and lift coefficient $C_y = 2$; and

https://doi.org/10.1017/jfm.2014.7 Published online by Cambridge University Press

(*c*) optimized trajectory VI, a bird-like case, with specified thrust coefficient $C_x = 1$ and lift coefficient $C_y = 4$.

As noted in table 1, Trajectories I, II, and III represent non-optimized examples using simple sinusoidal definitions for the motion trajectory.

In optimized trajectory IV ($C_x = 1$ and $C_y = 0$), corresponding to substantial thrust and near-zero transverse force, particle image velocimetry shows that in each cycle of oscillation the leading- and trailing-edge vortices are manipulated by the foil trajectory to form a pair with their centres lined up along the axial direction, hence providing a strong jet without sideways forces (figure 12). This wake is analogous to that of a pulsed jet or the drag-based thrust from a paddle, yet the force remains lift-based and efficient because the in-line motion rotates the direction of the relative foil–fluid velocity. Small additional vortices can also be shed as the foil quickly rotates at the beginning of the downstroke. The optimization process minimizes the strength of secondary vortices primarily through changes in the angle of attack profile. The final thrust efficiency is comparable to symmetric flapping foil propulsion at similar maximum angle of attack.

In optimized trajectory V ($C_x = 0$ and $C_y = 2$), corresponding to substantial transverse force and near-zero thrust force, PIV shows that the leading-edge vortex remains attached to the foil over a large part of a cycle, while producing substantial force, and then interacts destructively with part of the trailing-edge vortical patterns. Some of the trailing-edge vorticity lies at a distance from the leading-edge vortex, avoiding the destructive interference. Hence, in the far wake the dominant vorticity resembles the starting vortex forming in an impulsively accelerating foil.

Optimized trajectory VI ($C_x = 1$ and $C_y = 4$) corresponds to substantial transverse force combined with a smaller thrust force. PIV provides a wake image that combines features of Optimized Trajectories IV and V, namely a pair of counter-rotating vortices that provide the thrust force and a starting foil-like isolated vortex produced by trailing-edge vorticity.

The present results have been derived for steady-state oscillations, or for oscillations that transition smoothly between modes from cycle to cycle (figure 2). However, the same procedure can be extended to apply to rapidly varying motions, such as those needed for manoeuvring, or for optimizing different performance metrics other than σ^*. Additionally, unsteady forces on a freely moving body will affect the body velocity U, requiring further corrective optimization of the flapping foil actuator. However, minimizing the oscillation cost σ^* incurs the benefit of minimizing the oscillation in U perpendicular to the mean motion of travel, and such corrections fit within our procedures.

Our results are for high-aspect-ratio foils moving within a stroke plane, towed at a constant velocity, in order to elucidate the principal effects of the in-line motion. An extension for three-dimensional foil kinematics, using for example the methods of Thomas *et al.* (2004), would be the next step in order to provide further insight into animal flight and swimming. Deviations from the stroke plane need to be studied as well as they are known to also have an effect on the performance of the foil (Sane & Dickinson 2001; Viswanath & Tafti 2012).

Acknowledgements

The authors wish to thank H. Beem, S. Steele, and L. Mendelson for their aid in conducting experiments. Moreover, we also wish to thank A. Barry, Dr G. Weymouth,

https://doi.org/10.1017/jfm.2014.7 Published online by Cambridge University Press

and the entire MIT Towing Tank group for their thoughtful discussions on hydrodynamics and optimization.

The authors wish to acknowledge funding support from SMART, the Singapore-MIT Alliance for Research and Technology, within the CENSAM program; and from the MIT Sea Grant Program (contract number NA10OAR410086). We further acknowledge additional fellowship support from the NSF Graduate Research Fellowships Program. This research was also conducted with Government support under and awarded by DoD, Air Force Office of Scientific Research, National Defense Science and Engineering Graduate (NDSEG) Fellowship, 32 CFR 168a.

REFERENCES

ANDERSON, J. M., STREITLEIN, K., BARRETT, D. S. & TRIANTAFYLLOU, M. S. 1998 Oscillating foils of high propulsive efficiency. *J. Fluid Mech.* **360**, 41–72.

BERG, A. M. & BIEWENER, A. A. 2010 Wing and body kinematics of takeoff and landing flight in the pigeon (columba livia). *J. Expl Biol.* **213** (10), 1651–1658.

DAVENPORT, J., MUNKS, S. A. & OXFORD, P. J. 1984 A comparison of the swimming of marine and freshwater turtles. *Proc. R. Soc. Lond.* B **220** (1221), 447–475.

DICKINSON, M. H. & GOTZ, K. G. 1993 Unsteady aerodynamic performance of model wings at low Reynolds numbers. *J. Expl Biol.* **174** (1), 45–64.

DILEO, C. & DENG, X. 2009 Design of and experiments on a dragonfly-inspired robot. *Adv. Robot.* **23** (7–8), 1003–1021.

EPPS, B. P. & TECHET, A. H. 2007 Impulse generated during unsteady maneuvering of swimming fish. *Exp. Fluids* **43** (5), 691–700.

GILL, P. E., MURRAY, W. & SAUNDERS, M. A. 2005 SNOPT: an SQP algorithm for large-scale constrained optimization. *SIAM Rev.* **47** (1), 99–131.

HANSEN, N. & OSTERMEIER, A. 2001 Completely derandomized self-adaptation in evolution strategies. *Evol. Comput.* **9** (2), 159–195.

HEDENSTRÖM, A., JOHANSSON, L. C. & SPEDDING, G. R. 2009 Bird or bat: comparing airframe design and flight performance. *Bioinspir. Biomim.* **4** (1), 015001.

HOVER, F. S., HAUGSDAL, Ø. & TRIANTAFYLLOU, M. S. 2004 Effect of angle of attack profiles in flapping foil propulsion. *J. Fluids Struct.* **19** (1), 37–47.

JABRI, M. & FLOWER, B. 1992 Weight perturbation: an optimal architecture and learning technique for analog VLSI feedforward and recurrent multi-layer networks. *IEEE Trans. Neural Networks* **3**, 154–157.

KAYA, M. & TUNCER, I. H. 2007 Nonsinusoidal path optimization of a flapping airfoil. *AIAA J.* **45** (8), 2075–2082.

KERN, S. & KOUMOUTSAKOS, P. 2006 Simulations of optimized anguilliform swimming. *J. Expl Biol.* **209** (24), 4841–4857.

KOEKKOEK, G., MUIJRES, F. T., JOHANSSON, L. C., STUIVER, M., VAN OUDHEUSDEN, B. W. & HEDENSTRÖM, A. 2012 Stroke plane angle controls leading edge vortex in a bat-inspired flapper. *C. R. Méc.* **340** (1–2), 95–106.

LICHT, S. C., WIBAWA, M. S., HOVER, F. S. & TRIANTAFYLLOU, M. S. 2010 In-line motion causes high thrust and efficiency in flapping foils that use power downstroke. *J. Expl Biol.* **213** (1), 63–71.

LINDHE NORBERG, U. M. & WINTER, Y. 2006 Wing beat kinematics of a nectar-feeding bat, Glossophaga soricina, flying at different flight speeds and Strouhal numbers. *J. Expl Biol.* **209** (19), 3887–3897.

MARESCA, C., FAVIER, D. & REBONT, J. 1978 Experiments on an aerofoil at high angle of incidence in longitudinal oscillations. *J. Fluid Mech.* **92** (4), 671–690.

MOORED, K. W., DEWEY, P. A., SMITS, A. J. & HAJ-HARIRI, H. 2012 Hydrodynamic wake resonance as an underlying principle of efficient unsteady propulsion. *J. Fluid Mech.* **708**, 329–348.

https://doi.org/10.1017/jfm.2014.7 Published online by Cambridge University Press

NUDDS, R. L., TAYLOR, G. K. & THOMAS, A. L. R. 2004 Tuning of Strouhal number for high propulsive efficiency accurately predicts how wingbeat frequency and stroke amplitude relate and scale with size and flight speed in birds. *Proc. R. Soc. Lond.* B **271** (1552), 2071–2076.

PAN, Y., DONG, X., ZHU, Q. & YUE, D. K. P. 2012 Boundary-element method for the prediction of performance of flapping foils with leading-edge separation. *J. Fluid Mech.* **698**, 446–467.

PREMPRANEERACH, P., HOVER, F. S. & TRIANTAFYLLOU, M. S. 2003 The effect of chordwise flexibility on the thrust and efficiency of a flapping foil. In *Proc. 13th Intl Symp. on Unmanned Untethered Submersible Technology: Special Session on Bioengineering Research Related to Autonomous Underwater Vehicles*, New Hampshire.

READ, D. A., HOVER, F. S. & TRIANTAFYLLOU, M. S. 2003 Forces on oscillating foils for propulsion and maneuvering. *J. Fluids Struct.* **17**, 163–183.

ROBERTS, J. W., MORET, L., ZHANG, J. & TEDRAKE, R. 2010 Motor Learning at Intermediate Reynolds Number: Experiments with Policy Gradient on the Flapping Flight of a Rigid Wing. In *From Motor to Interaction Learning in Robots* vol. 264, p. 293, Springer.

SANE, S. P. & DICKINSON, M. H. 2001 The control of flight force by a flapping wing: lift and drag production. *J. Expl Biol.* **204** (15), 2607–2626.

SCHOUVEILER, L., HOVER, F. & TRIANTAFYLLOU, M. 2005 Performance of flapping foil propulsion. *J. Fluids Struct.* **20** (7), 949–959.

SLAOUTI, A. & GERRARD, J. H. 1981 An experimental investigation of the end effects on the wake of a circular cylinder towed through water at low Reynolds numbers. *J. Fluid Mech.* **112**, 297–314.

SZYMIK, B. G. & SATTERLIE, R. A. 2011 Changes in wingstroke kinematics associated with a change in swimming speed in a pteropod mollusk, Clione limacina. *J. Expl Biol.* **214** (23), 3935–3947.

TAYLOR, G. K., NUDDS, R. L. & THOMAS, A. L. R. 2003 Flying and swimming animals cruise at a Strouhal number tuned for high power efficiency. *Nature* **425** (October), 707–711.

THEODORSEN, T. 1935 General theory of aerodynamic instability and the mechanism of flutter. *NACA Tech. Rep.* 496.

THOMAS, A. L. R., TAYLOR, G. K., SRYGLEY, R. B., NUDDS, R. L. & BOMPHREY, R. J. 2004 Dragonfly flight: free-flight and tethered flow visualizations reveal a diverse array of unsteady lift-generating mechanisms, controlled primarily via angle of attack. *J. Expl Biol.* **207** (24), 4299–4323.

TOBALSKE, B. & DIAL, K. 1996 Flight kinematics of black-billed magpies and pigeons over a wide range of speeds. *J. Expl Biol.* **199** (2), 263–280.

TOBALSKE, B. W., WARRICK, D. R., CLARK, C. J., POWERS, D. R., HEDRICK, T. L., HYDER, G. A. & BIEWENER, A. A. 2007 Three-dimensional kinematics of hummingbird flight. *J. Expl Biol.* **210** (13), 2368–2382.

TRIANTAFYLLOU, G. S., TRIANTAFYLLOU, M. S. & GROSENBAUGH, M. A. 1993 Optimal thrust development in oscillating foils with application to fish propulsion. *J. Fluids Struct.* **7** (2), 205–224.

TRIANTAFYLLOU, M. S., TRIANTAFYLLOU, G. S. & GOPALKRISHNAN, R. 1991 Wake mechanics for thrust generation in oscillating foils. *Phys. Fluids* A **3** (12), 28–35.

VISWANATH, K. & TAFTI, D. K. 2012 Effect of stroke deviation on forward flapping flight. *AIAA J.* **51** (1), 145–160.

WAGNER, H. 1925 Über die entstehung des dynamischen auftriebes von tragflügeln. *Z. Angew. Math. Mech.* **5** (1), 17–35.

WAKELING, J. M. & ELLINGTON, C. P. 1997 Dragonfly flight. ii. velocities, accelerations and kinematics of flapping flight. *J. Expl Biol.* **200** (3), 557–582.

https://doi.org/10.1017/jfm.2014.7 Published online by Cambridge University Press